This is to certify that the

thesis entitled

EFFECT OF PLASMA ENERGY, PLASMA POWER, WORKING DISTANCE, AND
INERT GAS PRESSURE ON COMPOSITION OF SPUTTERED THERMOELASTIC
TITANIUM-NICKEL THIN FILMS

presented by

Jiun-Chung Lee

has been accepted towards fulfillment
of the requirements for

Master's degree in Materials Science

Major professor

Date August 17, 1994

DATE DUE	DATE DUE	DATE DUE
~~MAY 0 7 1998~~ ~~JUN 0 3 1998~~		
~~MAR 0 3 1999~~		
~~JUL 0 1 2000~~		

EFFECT OF PLASMA ENERGY, PLASMA POWER, WORKING DISTANCE, AND INERT GAS PRESSURE ON COMPOSITION OF SPUTTERED THERMOELASTIC TITANIUM-NICKEL THIN FILMS

By

Jiun-Chung Lee

A THESIS

Submitted to
Michigan State University
in partial fulfillment of the requirements
for the degree of

MASTER OF SCIENCE

Department of Materials Science and Mechanics

1994

ABSTRACT

EFFECT OF PLASMA ENERGY, PLASMA POWER, WORKING DISTANCE, AND INERT GAS PRESSURE ON COMPOSITION OF SPUTTERED THERMOELASTIC TITANIUM-NICKEL THIN FILMS

By

Jiun-Chung Lee

Thin films of TiNi are of interest for application to shape-memory microactuators. The transformation temperature of TiNi shape memory alloys is extremely sensitive to the alloy composition. Increasing the Ni content beyond stoichiometry decreases the transformation temperature by approximately 100 K per 1 at% Ni. Therefore, to maintain reasonable control over transformation temperature, it is desirable to control film composition to within ± 0.1 at%. The present study has focused on the effect of sputter deposition process variables on composition in TiNi thin films.

By adjusting the process variables, thin films with compositions showing positive and negative deviations from the target-alloy composition have been obtained. It was found that the plasma power had a critical effect on the films composition, although the plasma voltage and gas pressure also affected it. The results are understood in terms of the sputtering yield of alloy constituent elements and the mean free path of energetic neutral atoms in the plasma.

ACKNOWLEDGMENTS

I would like to give thanks to several important people.

To Dr. Grummon, my major professor, who through his knowledge and guidance made this study successful.

To Liuwen Chang for his initiative on the study of sputter-deposited TiNi film composition.

To Seungho Nam for his constant help on the experimental technology.

To Zhiwei Cai for the patient instruction on the use of the SEM and composition analysis.

To Li Ho for his effort on the maintenance of the sputtering system.

To Alan Gibon for his help on the thesis writing.

And to my parents, their constant support and substantial financial contributions, made my education possible.

TABLE OF CONTENTS

LIST OF TABLES

LIST OF FIGURES

CHAPTER 1 INTRODUCTION

Shape memory properties in the TiNi alloys were first discovered in the 1960's at the Naval Ordnance Laboratory [1]. Since that time, extensive studies have been devoted to the development and application of bulk TiNi alloys. The shape-memory effect (SME) is due to the thermoelastic martensitic phase transformations at a given transition temperature. Thus, the phase transformation temperatures are the most important properties of TiNi shape memory alloys because they determine the working temperature range of the materials. Since the transformation temperature for TiNi alloy is very sensitive to the alloy composition [2], precise composition control in the deposition process is essential.

TiNi alloys have been used in thin film form as the material basis for microactuators in microelectromechanical systems, and as surface microalloys for structural metals [3, 4]. Usually, alloy thin films are fabricated by a physical vapor deposition process such as sputtering or evaporation. In the present study, TiNi thin films were deposited by a single-target dc magnetron sputtering system in an argon atmosphere. Sputtering was chosen a means for producing films because it is recognized to be the most reliable method for control of composition [5]. However, the composition of a sputter-deposited TiNi film can be quite different from that of the sputtering target because of the different process parameters, such as distance between target and substrate, gas pressure, plasma potential (voltage), and substrate temperature. Nevertheless, the composition change should be reproducible for a given set of conditions. Therefore, the composition in the deposited films are functions of the process variables.

Studies on TiNi thin films have been reported previously. Most of them have been concerned with the mechanical and metallurgical properties of thin films. The objective of the present work is to determine the working conditions under which the compositions of TiNi thin films can be made to show both positive and negative deviations from the TiNi target alloy composition. This is desirable so that small, well-controlled deviations from stoichiometry can be made using a single stoichiometric target which is stable with respect to precipitation of intermetallic precipitates. The significance of the effect of various process variables on the composition change are surveyed. Through this study, a precise knowledge of the relationship between thin film composition and sputter deposition process parameters can be obtained. Furthermore, using this relationship, it is easy to fabricate TiNi thin films with desired composition by adjusting the process parameters.

CHAPTER 2 LITERATURE REVIEW

2.1 TiNi Shape Memory Alloys

2.1.1 Shape Memory Properties

TiNi alloys are ordered intermetallic compounds based on the equiatomic composition [6]. They experience a crystallographically reversible martensitic phase transformation causing the Shape Memory Effect (SME). The SME can be described with reference to the cooling and heating curves in Figure 2-1 [7]. There is no change in the shape of a specimen cooled from above austenite finish temperature (A_f) to below martensite finish temperature (M_f). When the specimen is deformed below M_f, it remains so deformed until it is heated. The shape recovery begins at the austenite start temperature (A_s) and is completed at the austenite finish temperature (A_f). At the inflection point between A_s and A_f, about 50% of original shape is recovered. Also, the application of stress can induce the martensitic phase transformation within a certain temperature interval. The large anelastic strain (~ 5%) associated with the stress-induced transformation is recoverable upon unloading, which give rise to the superelastic effect (SE).

2.1.2 Phase Stability and Occurrence in TiNi Alloys

From the TiNi phase diagram, as shown in Figure 2-2 [8], stoichiometric TiNi phase exists at high temperature, with a steep solvus boundary on the Ti-rich side, slight solubility for nickel, and only one intermetallic phase Ni_3Ti on the Ni-rich side. The diagram has traditionally showed an eutectoid decomposition ($TiNi \rightarrow Ti_2Ni + Ni_3Ti$) at 903 K. However, Wasilewski *et al.* [9] proposed that the TiNi may remain to be a stable phase down to room temperature with a very narrow stoichiometric range, as indicated in Figure 2-3 [9]. Furthermore, Van Loo *et al.* [10], Nishida *et al.* [11] and Kim *et al.* [12] reported the existence of metastable phases other than Ni_3Ti on the Ni-rich side, such as Ni_3Ti_2 and $Ni_{14}Ti_{11}$. Also, Saburi *et al.* [13] proposed that it might be more appropriate to express $Ni_{14}Ti_{11}$ as a Ni_4Ti_3 phase based on the crystal structure. The equilibrium phase diagram on the Ni-rich side for the low temperature range, however, is not well established and controversy on the composition and structure of those phases exists. Most researchers accept that the microstructures of TiNi alloys are primarily single phase, with small amounts of other phases distributed throughout the matrix. Since the precipitate phases are generally isomorphous with TiNi, they produce coherency strains which profoundly affect transformation characteristics, as well as strength and ductility.

Melton [6] also pointed out that the presence of oxygen affects the microstructure of TiNi alloys. According to the Ni-Ti-O phase diagram, Figure 2-4 [14], oxygen decreases the stoichiometric range of the TiNi phase and can terminate compositions within a three phase region consisting of TiNi, $Ti_4Ni_2O_x$ and Ni_3Ti. Thus, the Ni_3Ti phase can be present in a Ti-rich alloy and Ti_2Ni is sometimes found in Ni-rich alloys. Besides, the oxide $Ti_4Ni_2O_x$ is isostructural with the intermetallic Ti_2Ni, which has a lattice parameter increasing slightly from 1.132 nm (Ti_2Ni) to 1.134 nm ($Ti_4Ni_2O_x$). This makes the identification of unique phases very difficult.

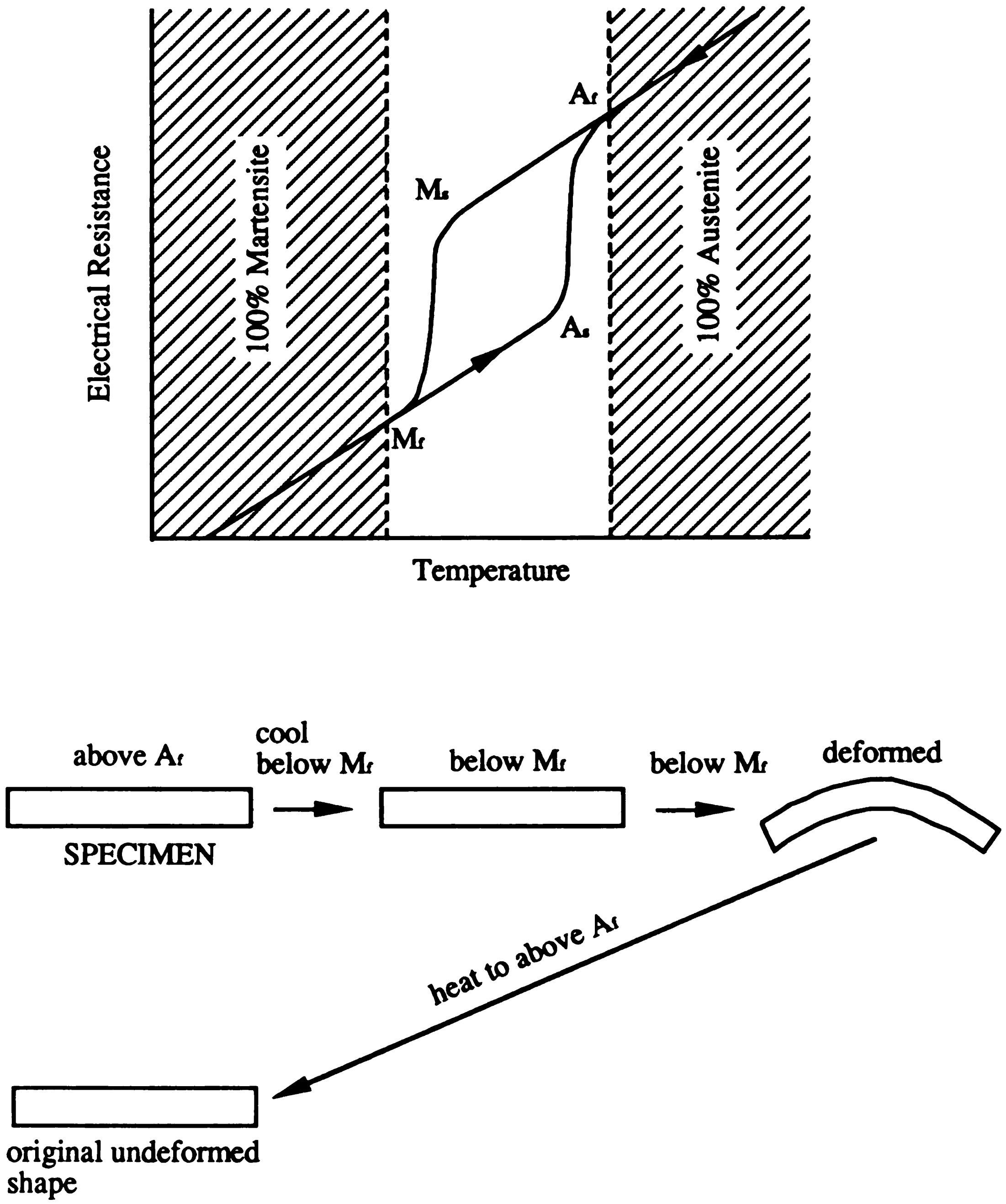

Figure 2-1 The shape memory effect is described with reference to a plot of electrical resistance vs. temperature from which the characteristic transformation temperature M_f, M_f, A_f and A_f are determined [7].

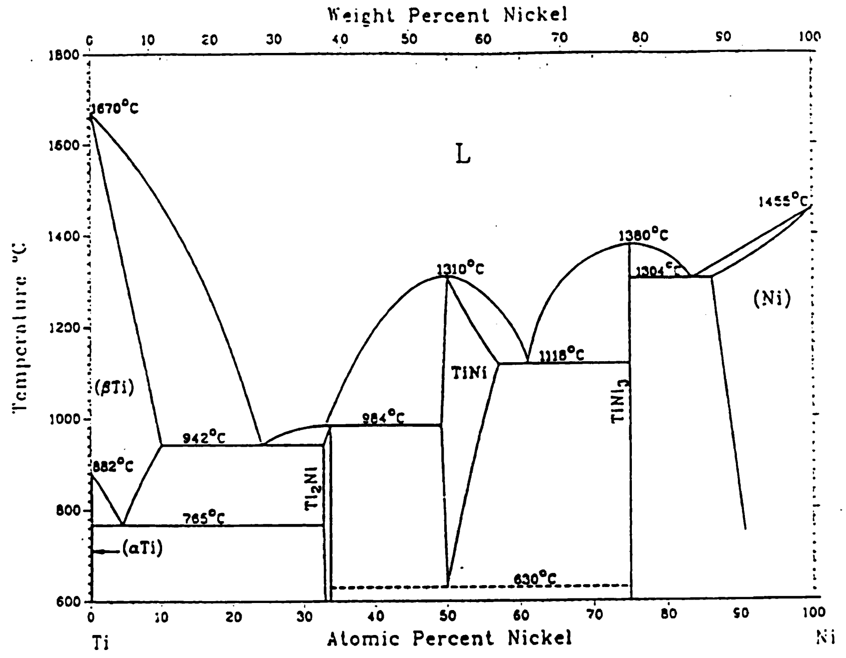

Figure 2-2 Equilibrium Phase Diagram for TiNi Alloys [8]

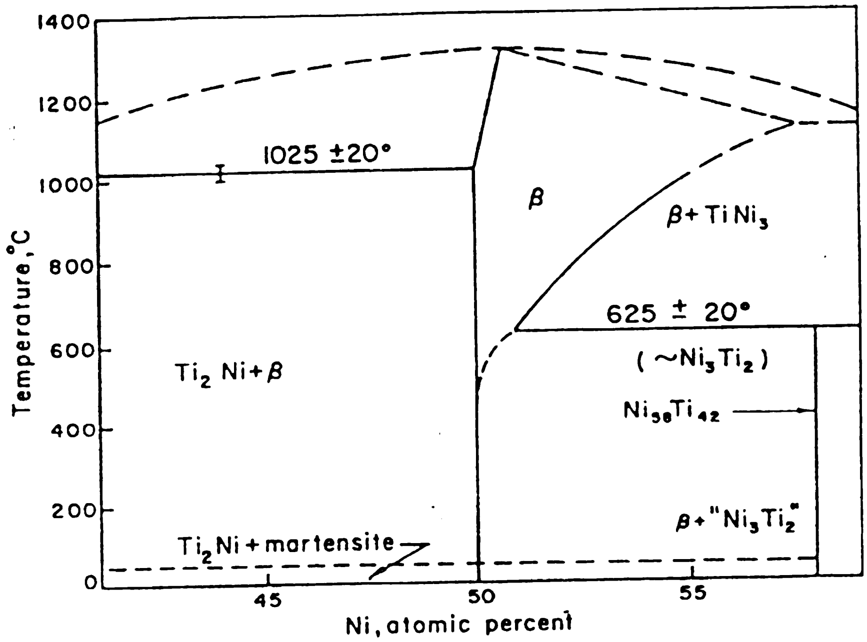

Figure 2-3 Proposed equilibrium diagram of the Ti-Ni binary system in the vicinity of the equiatomic composition at low temperature [9].

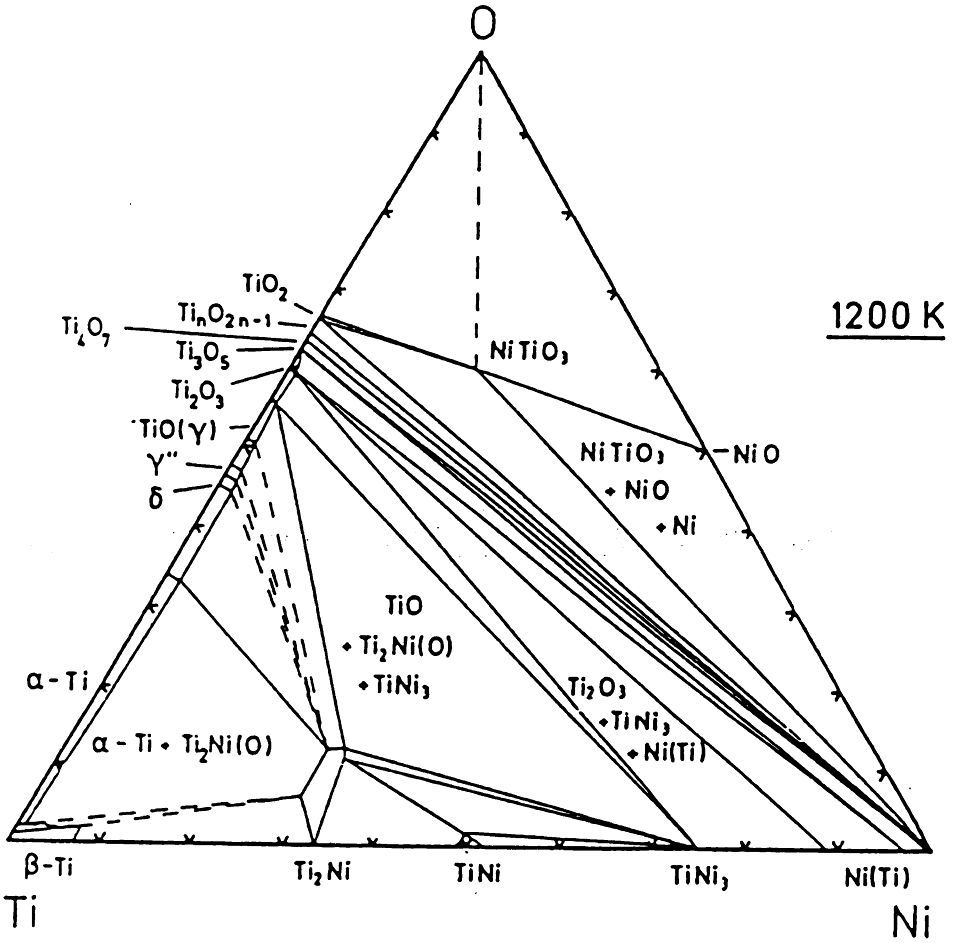

Figure 2-4 Isothermal Cross Section Through the Ti-Ni-O Phase Diagram at 1200 K [14]

2.1.3 The Effects of Alloy Composition on The Transformation Temperature

The martensite start temperature (M_s) depends strongly on composition, particularly on the Ni-rich side, as shown in Figure 2-5 [6]. The M_s temperature changes over 100 K/at% on the Ni-rich side, whereas the change is only about 20 K/at% on the opposite side. On the Ti-rich side, the solubility range is almost independent of temperature. Therefore, Ti-rich alloys show less sensitivity primarily as a result of the formation of a Ti-rich precipitate (Ti_2Ni), leaving the matrix composition essentially TiNi.

The strong dependence of M_s on composition on the Ni-rich side is a consequence of higher Ni solubility at temperatures above around 773 K. Dissolved nickel may then precipitate out upon aging for longer times at lower temperatures. The first factor affecting the M_s is that the precipitation of Ni-rich phases leads to a more Ti-rich matrix composition, with higher M_s. The second factor is that the internal stress fields associated with semi-coherent precipitates, such as Ni_4Ti_3, have a strong effect on suppressing the M_s temperature and constraining the further development of martensite [15]. Similar results have been found when dislocations are introduced by cold work or transformation cycling [16].

In addition, substituting 3d transition metals (such as Fe, Co, or Cr), and Cu, for Ni has a great effect on the phase transformation behavior of TiNi alloys [2]. In these cases, the effects are due to the incorporation of these elements into the lattice structure itself and transformation temperatures are shifted. Also, the existence of interstitial impurities like C, O, N, or H, which either form compound phases or exist inside the lattice, will decrease the transformation temperature dramatically.

Therefore, to maintain the best control over the transformation temperature, precise composition control and avoidance of contamination by O or N are required when fabricating the TiNi alloys. Depending upon the desired M_s, the necessary composition control is to between one tenth and one hundredth of an atomic percent.

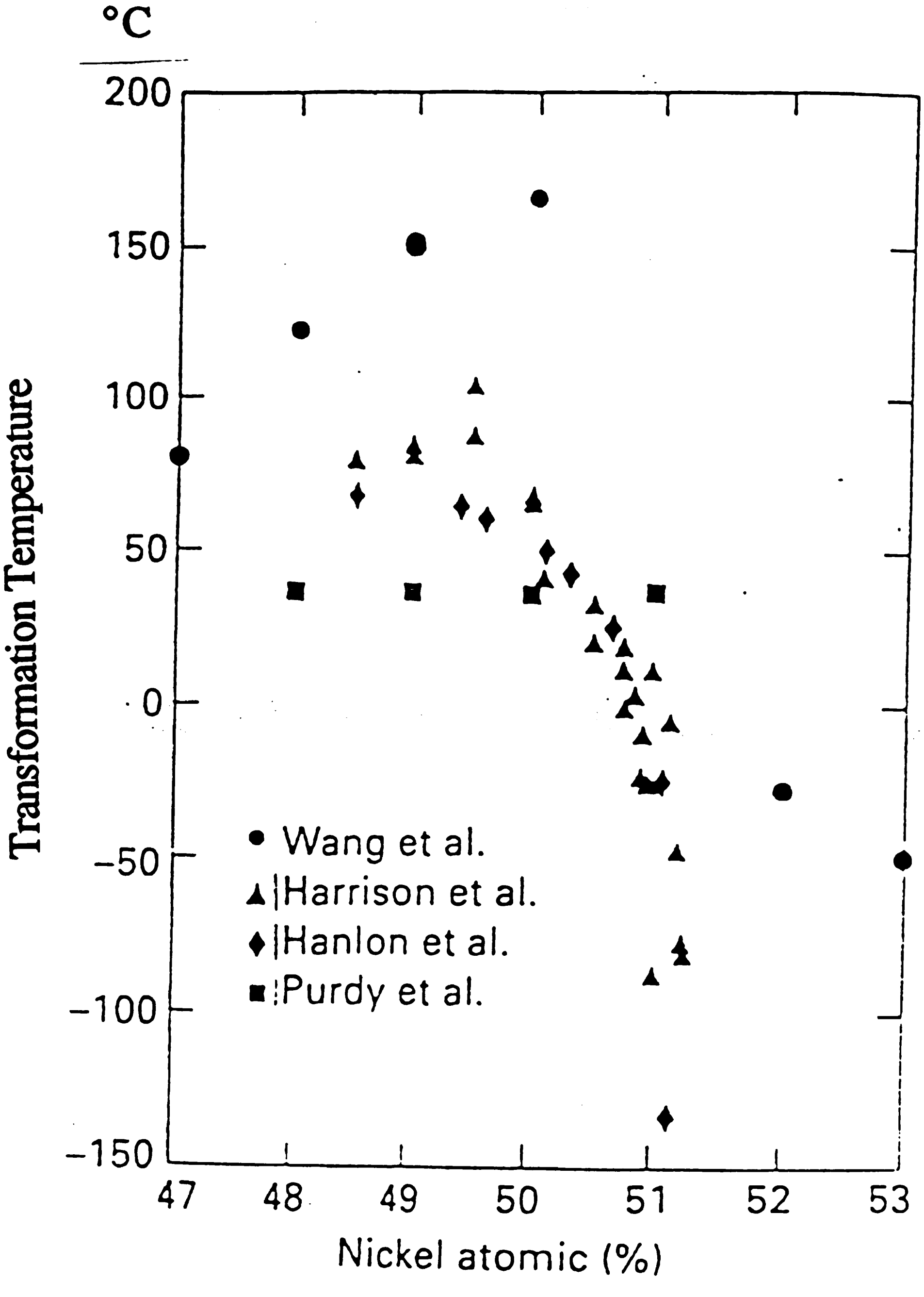

Figure 2-5 The Dependence of the Transformation Temperature (M_s) on Nickel Content in TiNi Alloys [6]

2.2 Mechanical & Metallurgical Studies of TiNi Thin Films

TiNi alloys not only possess shape memory and superelasticity effects, but also provide high ductility, superior corrosion resistance, fatigue resistance, and high damping capacity. Consequently, they have been used as high force actuators [17], tubing connectors [18], and orthodontic hardware [19]. In addition to development of microactuators in microelectromechanical systems, TiNi thin films have attracted attention for potential application as a superelastic surface coatings to improve fatigue or erosion resistance [3, 4].

TiNi thin films with near-equiatomic overall compositions have been fabricated by various methods, and their properties have been studied [20-32]. Thin films formed by vapor condensation in binary systems were predicted to be amorphous. Solid state immisciblity and a large difference (greater than 10%) in the atomic radii of the constituents were the most important ingredients for amorphous phase formation [20]. However, a structural difference rule has been proposed for amorphization by ion beam mixing. According to this rule, the structural difference between the constituent elements of the binary systems, rather than the radii or electronegativity difference, dictates amorphous phase formation [21].

High energy ion irradiation has been employed to mix bilayered nickel and titanium deposited by electron beam evaporation. Rai *et al.* [22] reported that an amorphous TiNi layer was formed after ion-mixing. Ion beam sputtering and ion beam enhanced deposition were other methods to make TiNi thin films [4, 23]. The common advantage for electron beam and ion beam processes is low process pressure. They can be operated at low background pressure (~ 10^{-4} Pa) which results in less inclusion of gas molecules in the sputtered films and less scattering of the sputtered particles during transit. The disadvantage is that it is difficult to obtain a reproducible compositional results even at the same process conditions.

Periodic multilayers of nickel and titanium deposited by dual magnetron sputtering were studied by Clemens [24]. The structures of sputter-deposited multilayer TiNi films are strong functions of sputtering pressure. Low sputter pressure (~ 0.27 Pa) leads to relatively high quality, textured crystalline layers. High sputter pressure (~ 1.36 Pa) results in random orientation and poor layering, caused by island nucleation and growth. This effect is due to that increase in pressure causing lower impact energy of the deposited species, which results in lower atomic mobility. Amorphous TiNi thin films with compositions of $Ni_{30}Ti_{70}$, $Ni_{56}Ti_{44}$ and $Ni_{68}Ti_{32}$ were also prepared by planar magnetron sputtering [12]. The crystallization behavior of these thin films were surveyed. For the near-equiatomic thin film (i.e. $Ni_{56}Ti_{44}$), complicated crystallization sequences and many different precipitate phases were observed.

A triode magnetron sputtering method was adopted by Chang [25, 26] to fabricate single layer (SL) of Ti(NiCu) and periodic multilayered (PML) of Ti(NiCu) and Ti thin films. Their compositions, crystallographies, interface coherency and corresponding transformation behavior were studied. In compositional results, a severe Ti depletion, relative to the sputter-target composition, was found in the SL films. The reason causing this phenomenon was believed that the growing films were bombarded by energetic species, resulting in preferential resputtering. According to the published sputtering yield data of elemental Ni and Ti [40], Ni shows higher sputtering yield than Ti at the same bombarding energy. Thus, a Ni depletion, produced by preferential resputtering, is expected in the growing film. However, the Ti loss found in the SL films in Chang's studies indicated that the sputtering properties of Ni and Ti in amorphous TiNi alloys may be different from pure elements and crystallized TiNi target alloys.

Ion beam assisted deposition (IBAD) experiments were thus designed by Chang [26] to gain better understanding of the sputtering behavior of Ti and Ni in amorphous TiNi alloys. The Ti depletion is plotted as a function of ion-to-atom (I/A) arrival ratio, shown in Figure 2-6. The results showed that a general trend of Ti depletion in the IBAD processed films which increased with increasing of I/A ratio. Also, a dramatic increase of the sputtering yield ratio $Y = Y_{Ti}/Y_{Ni}$ is found at low assist-beam energy. In the low energy regime (~ 50 eV), the sputtering rate is extremely sensitive to the variation of ion energies (E_i) and energy of sputtering threshold (E_{th}) [27] (threshold energy, the minimum requirement energy for sputtering). Since Ni has a higher threshold energy than Ti, as shown in Table 2-1 [28], the increase of sputtering yield ratio can explain high Ti depletion rate for the 50 eV assisted-beam energy. Chang [26] concluded that the relation of the sputtering yields of Ni and Ti in binary amorphous TiNi alloys can be expressed as $Y_{Ti} > Y_{Ni}$ in low and intermediate energy regimes (< 500 eV), and the sputtering yield ratio of Ti and Ni in amorphous TiNi alloys increased from 1.75 at 500 eV to about 9 at 50 eV of Ar bombarding ions.

Table 2-1 Threshold Energies (eV) [28]

	Ne	Ar	Kr	Xe	Hg
Al	13	13	15	18	18
Ti	22	**20**	17	18	25
V	21	23	25	28	25
Cr	22	22	18	20	23
Fe	22	20	25	23	25
Co	20	25	22	22	
Ni	23	**21**	25	20	
Cu	17	17	16	15	20
Nb	27	25	26	32	
Mo	24	24	28	27	32
Ag	12	15	15	17	
W	35	33	30	30	30
Pt	27	25	22	22	25
Au	20	20	20	18	

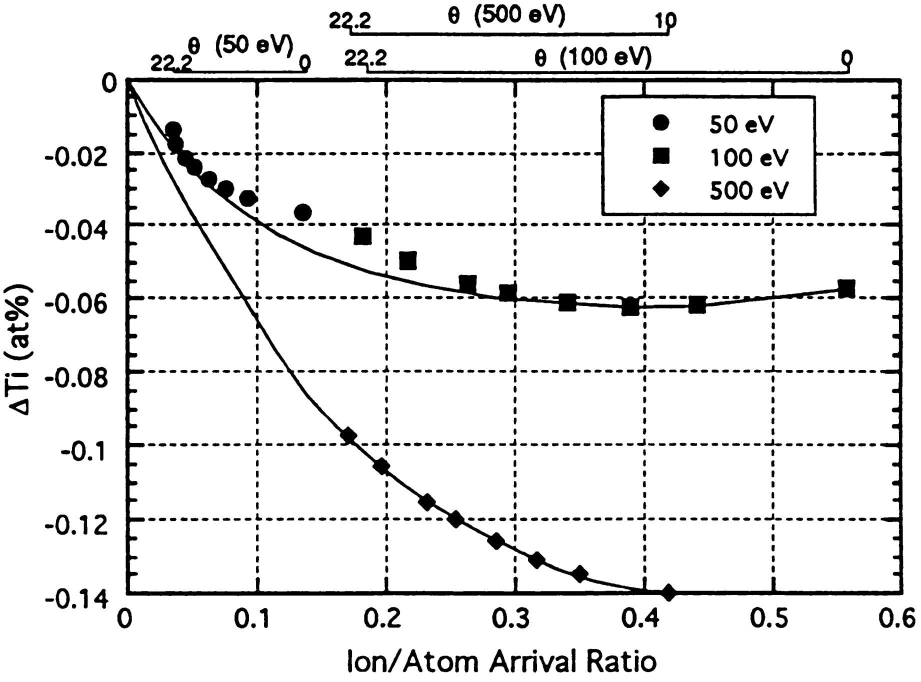

Figure 2-6 The change of Ti concentration of the IBAD processed TiNi films as a function of I/A ratio, relative to the expected composition of the film in the absence of an assist-beam. Data are shown for 50, 100, and 500 eV beam [26].

Since 1988, Busch, Johnson and his coworkers have conducted research on shape memory properties and applications in TiNi thin films [3, 29, 30]. TiNi thin films were deposited from an alloy target by dc magnetron sputtering. Sputtering targets were prepared from different compositions of TiNi alloys. One target with composition Ti - 50.1 at% Ni had a transition temperature of 303 K. The other target with composition Ti - 50.2 at % Ni had a transition temperature slightly above 373 K. The sputtering condition were: $P_{Ar} = 0.1$ Pa, $I = 0.5$ A, $V = 450$ V, source/target distance = 57 mm. After deposition, the resulting films were amorphous. Their crystallization temperatures were determined by Differential Scanning Calorimetry (DSC) and showed that the crystallization exotherm was located at about 753 K. Knowing the crystallization temperature, samples were vacuum encapsulated in quartz ampoules with a Ti sponge getter, annealed for 30 min at 823 K to ensure crystallization complete and air cooled. DSC was also used to identify and evaluate their phase transformations temperature behavior. It was found that the transformation temperatures of thin films were about 100 K lower than their target alloys. This phenomena was described as being the contamination of oxygen since oxygen can change the stability of TiNi phase. The composition of the target materials and the respective films were measured with the Flame Atomic Absorption method. Questions exist on the results: 1) the measured target compositions were significantly different from the nominal compositions; 2) the target alloys were richer in Ni than their thin film counterparts, but their transformation temperatures were higher. This differs from the general rule stating that as Ni concentration increases, M_s decreases. The reasons behind the results were not clarified.

Even though low transformation temperatures existed, the classical shape memory behavior was successfully demonstrated on TiNi thin films prepared by sputter deposition and a crystallization process. Two devices were designed by Johnson [3] using the SME of TiNi thin films: one is a microvalve and the other is microactuator, as shown in Figure 2-7 and Figure 2-8.

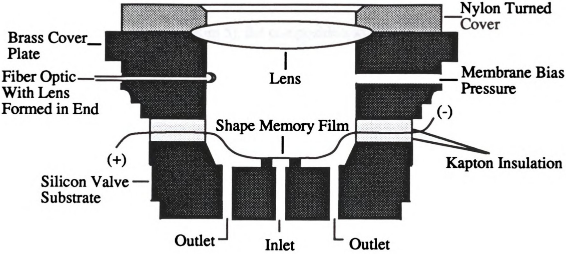

Figure 2-7 The Valve Design by Using TiNi Thin Films [3]

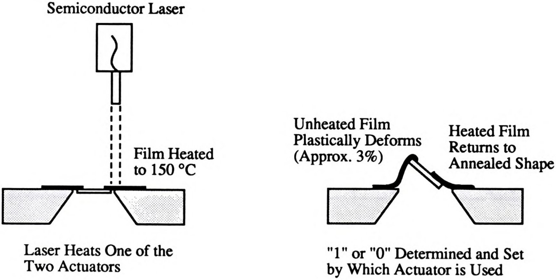

Figure 2-8 The Mirror Actuator Concept by Using TiNi Thin Films in [3]

Ishida *et al.* [31] used the rf magnetron sputtering method to fabricate TiNi thin films under different sputtering conditions. The advantages of rf magnetron sputtering over dc configuration will be discussed in Section 2.4.4. His compositional results were measured by electron-probe microanalyzer (EPMA) and shown in Table 2-2. Note that at low pressure process condition (Run 5), the composition was Ti depletion, too. This can strengthen the results in Chang's study [26]: at low Ar gas pressure, the resputtering of TiNi amorphous thin film resulted in the Ti loss in the thin films. Also, The mechanical properties of the annealed films were evaluated. They showed that the films formed at a high Ar gas pressure (13.3 Pa) exhibited poor mechanical properties due to the porous structure formed during sputtering. The films prepared at a low Ar gas pressure (0.67 Pa) exhibited a good shape memory behavior comparable with that of bulk TiNi alloys.

Table 2-2 Sputtering Conditions and Film Compositions in [31]

(Distance between target-substrate was 82 mm, and arget composition is Ti-50 at% Ni.)

Run	Ar gas Pressure	R.F Power	Substrate temperature	Film Composition (at%)	
	Pa	W	°K	Ti	Ni
1	13.3	400	523	50.2	49.8
2	6.7	600	573	50.5	49.5
3	6.7	400	523	50.6	49.4
4	6.7	200	523	51.6	48.4
5	0.67	400	523	48.6	51.4

Walker *et al.* [32] developed and demonstrated the deposition of thin film shape memory alloys and an associated dry etch, surface micromachining release process. The deposition and patterning procedure may be used for the materials and processing technology of silicon-based microelectronics. In addition, the activation and control of such structures is possible using currents and voltages compatible with standard IC electronic circuitry. However, the lack of detailed process flow makes the results suspect because the film should be amorphous in these experiments.

In summary, the research on TiNi thin films is drawing much attention and broad applications are developing. However, methods for fabricating thin films are critical since the transformation temperatures of TiNi alloys are extremely sensitive to Ti concentration. How to make a thin film with a precise composition control is the major concern in the fabrication processes. Sputtering is believed the best method to fabricate alloy thin films with close composition control. Nevertheless, the different process conditions for deposition will result in different composition results. The present work is designed to address on the relationship between process parameters and film compositions.

2.3 Deposition by Sputtering

Thin films can be fabricated by many methods, including thermal evaporation, sputtering, ion beam deposition and chemical vapor deposition. Among these methods, sputtering deposition has become one of the most versatile techniques in thin film technology for preparing thin solids films of almost any material because of the following advantages [33]:

(1) Sputtering can be accomplished from large-area targets, simplifying the problem of depositing films with uniform thickness over large substrates.

(2) Film thickness control is relatively easily achieved by selecting a constant set of operating conditions and then adjusting the deposition time to reach the desired film thickness.

(3) The alloy composition of sputter-deposited films can be more tightly controlled than that of evaporated films. This is especially important for alloys and compounds.

(4) Many important film properties, including stress and adhesion, can be controlled by altering process conditions, such as power and pressure.

(5) Once the process conditions are fixed, the same quality of thin films can be obtained repeatedly.

2.4 Principles of Sputtering

In general, sputtering is a term used to describe the mechanism by which atoms are dislodged from the surface of a material (target) by collision with energetic particles. These ejected atoms will condense on any solid substrate close to the target. The sputtering process consists of four steps: (a) ions are generated and directed at the target; (b) the ions sputter target atoms; (c) the ejected (sputtered) atoms are transported to the substrate, where; (d) they condense and form a thin film. It is important to note that the substrate may also be subject to energetic particle bombardment, and atoms may be sputtered from the substrate as well. It is in this context that differential sputtering rates complicate composition control.

2.4.1 Properties of Glow Discharge

The energetic particles used to strike target materials are generated by glow-discharge. A Glow-discharge is a self-sustaining type of plasma (a partially ionized gas containing an equal number of positive and negative charges, as well as a number of non-ionized neutral molecules) [33, 34, 35]. Figure 2-9 [34] is an illustration of the appearance of glow discharge for a simple dc diode type system. It consists of a glass tube which is evacuated and then filled with a gas at low pressure. Within the tube are two electrodes between which a dc potential difference is applied.

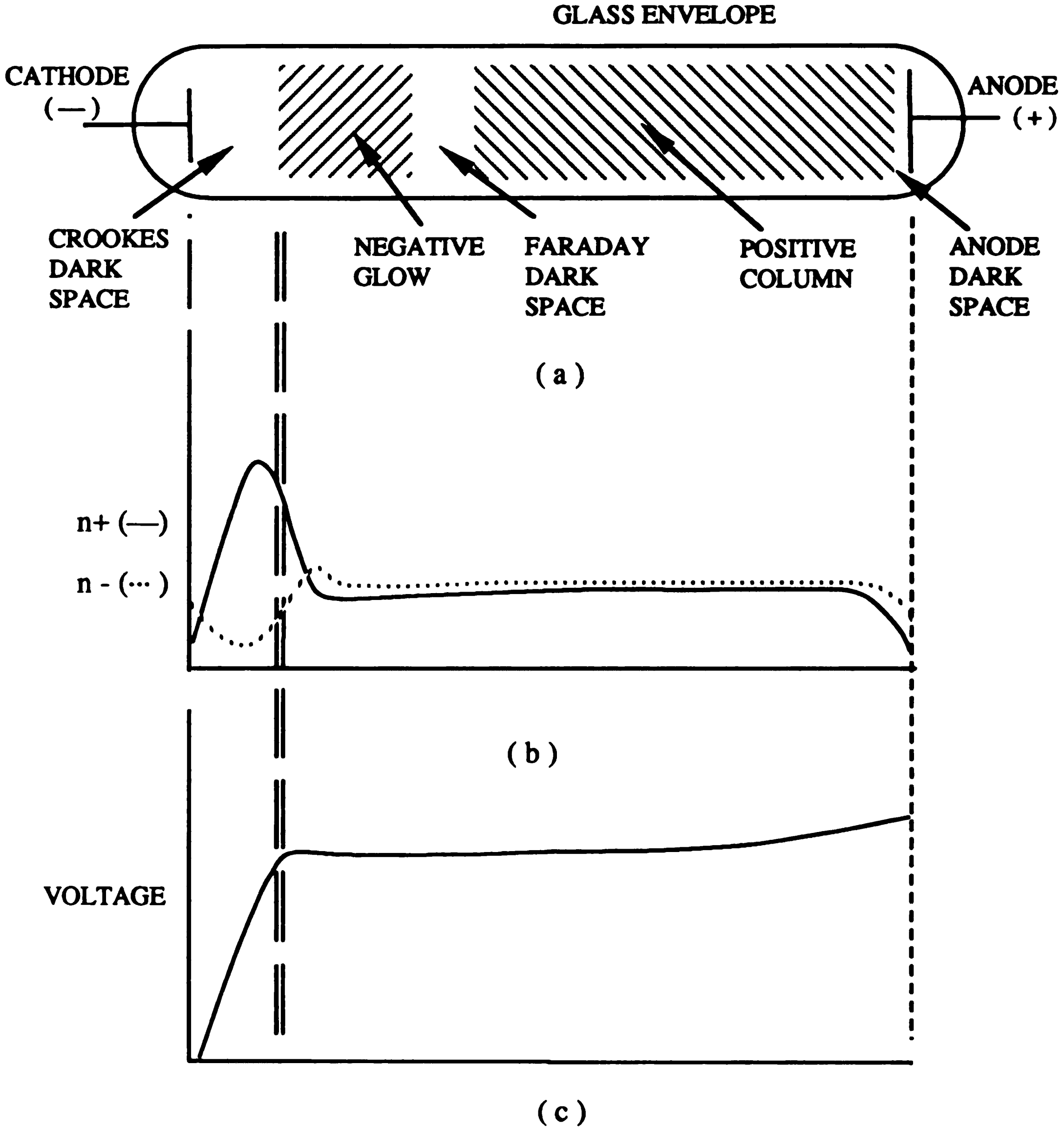

Figure 2-9 [34]

(a) Structure of a Glow Discharge in a D.C. Diode System

(b) Charged Particle Concentration in a Glow Discharge

(c) Voltage Variation in a D.C. Diode Glow Discharge

If a free electron is introduced into the tube (mostly likely created from the ionization of an argon atom by a passing cosmic ray), it will be accelerated by the electric field existing between the two electrodes. Then, it will pick up energy high enough to be transferred to the orbital electrons of the Ar atoms during an inelastic collision, causing their excitation or ionization. If the transferred energy is less than the ionization potential, the orbital electron will be excited to a higher energy state for a short time. The electron will then return to the ground state simultaneously emitting visible-light photons. Such excitation is the source of light emission in glow discharges. If the energy transferred is greater than the ionization potential, a second free electron (and positive ion) will be created. Subsequently, both free electrons will become accelerated again, thus cascading the number of free electrons creating a condition known as gas breakdown.

When the condition of gas breakdown is reached, electrons and ions are quickly lost to each of the electrodes and to all other surfaces within the chamber. Such loss processes include electron-ion recombination and an equivalent electron loss into the external circuit at the anode. Therefore, the current will decay to zero and glow discharge will extinguish unless there is a mechanism available for generating additional free electrons for sustaining the current flow. When a sufficient number of electrons are available to maintain the discharge, the discharge is said to be self-sustained.

The self-sustaining discharge has a particular structure, as shown in Figure 2-9a. The most important region of the discharge is the Crookes dark space between the negative glow and cathode. Any electrons near the cathode are rapidly accelerated away from it, due to their relatively light mass. The much more massive ions are accelerated toward the cathode, but much less quickly. Thus, on average, they spend more time than electrons traversing the Crookes dark space, and at any instant their concentration in the dark space is greater than that of electrons (The dark space can also be explained by the lower density of electrons, which causes lower excitation of atoms). This has the net effect of greatly increasing the electric field immediately in front of the cathode. As a result, the electric field in the remainder of the discharge is rather low and uniform. The greatest part of the voltage, between the anode and cathode, drops across the Crookes dark space so that charged particles experience their largest acceleration in this region.

When positive ions from the negative glow region enter the Crookes dark space, they experience the strong local electric field and become accelerated toward the cathode. They also have a high probability of exchanging their charge with neutral atoms in the dark space. In doing so, they retain their momentum, while losing their charge. The formerly neutral atom becomes an ion, and only at that moment does acceleration towards the cathode begin. Virtually no ions reach the target with the full dark space energy. In addition, this implies that the cathode is bombarded by energetic neutral atoms as well as energetic ions, and thus both species produce sputtering events.

The source of electrons that sustains the discharge is emission by the cathode of secondary electrons when struck by ions. When the electrons enter the dark space from the cathode, they are accelerated by the dark space and result in ionization. Then, new secondary electrons can be produced by ion bombardment of the cathode again. Thus, there only needs to be a sufficient number of ions produced in the dark space to produce enough secondary electrons to sustain the glow discharge.

If the pressure becomes too low (< 1.3 Pa), there are insufficient ionizing collisions between the electrodes, and the glow discharge extinguishes. Therefore, for the sputtering system to operate at pressures lower than 1.3 Pa, there should be another electron source or the ionizing efficiency of the available electrons should be increased, such as can be accomplished by the application of a magnetic field.

2.4.2 Physics of Sputtering

When a solid surface (target) is bombarded by atoms, ions, or molecules, many phenomena can occur, as shown in Figure 2-10 [34]. At very low energies (< 5 eV), ions are likely to be reflected or neutralized in the process. At much higher energies (> 10 keV), the impinging particles are most likely to be embedded in the target. This mechanism is the basis of ion implantation. At energies between the two extremes, some of the impinging ions may be responsible for the formation of an altered surface layer, i.e. structure rearrangement in the target material. Other ions result in a series of collision between atoms, leading to the ejection of one of these atoms from the surface into the gas phase (sputtering).

G.K. Wehner [36], whose theoretical work established a scientific basis for sputtering, often described sputtering as a game of three-dimensional billiards played with atoms, as shown in Figure 2-11. The sputtering process is compared to the "break" in a game of pool, in which the cue ball strikes the orderly arranged pack, scattering balls in all directions, including those going back to the player. Using this analogy, it is possible to realize how atoms may be ejected from a surface as the result of two binary collisions when a surface is struck by a particle with a velocity normal to the surface.

The sputtering yield, defined as the number of atoms ejected from the target surface per incident ion, is the most important parameter for characterizing the sputtering process. When the directions of sputtered atoms from the surface of polycrystalline materials are measured for the case of normal incidence, it is found that the directions of the ejected atoms leaving the surface essentially follow a cosine distribution. Evidently, in actual sputtering events, more than two collisions are involved, and the energy delivered is so randomly distributed that the effect of the incident momentum vector is lost. For the case when the surface is bombarded by ions at an oblique angle, there is a higher probability that the primary collision between the incident ion and the surface atom will lead to a sputtering event. Furthermore, oblique incidence confines the action closer to the surface, and thus sputtering is enhanced. Thus, the sputtering yield is a function of the incident angle with respect to the normal of target surface, as shown in Figure 2-12 [37]. It follows the sec(θ) curve and attains its maximum at θ of about 70°. This can be used to account for the different sputtering behavior for differing target morphologies.

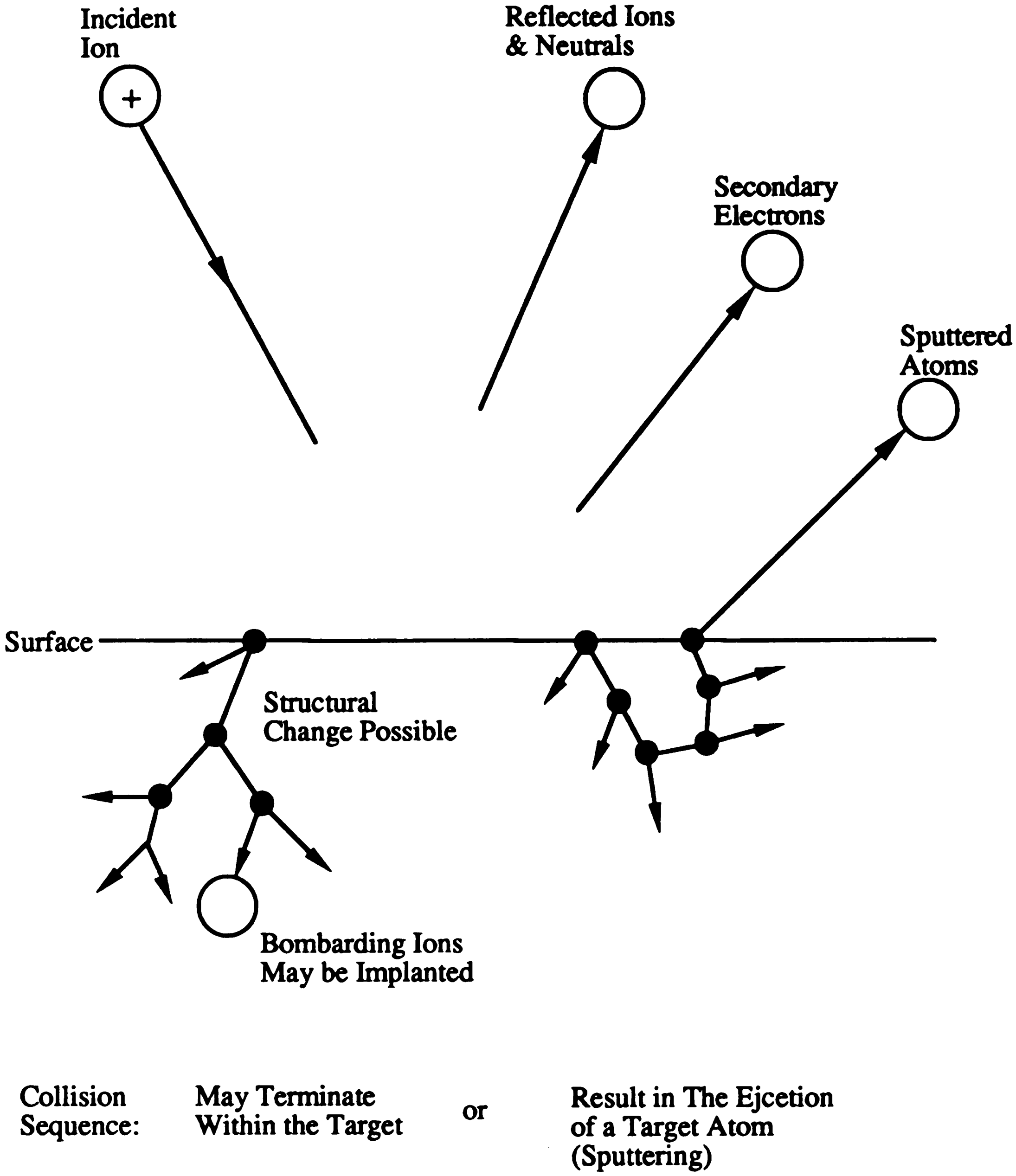

Figure 2-10 Interactions of Ions with the Surface [34]

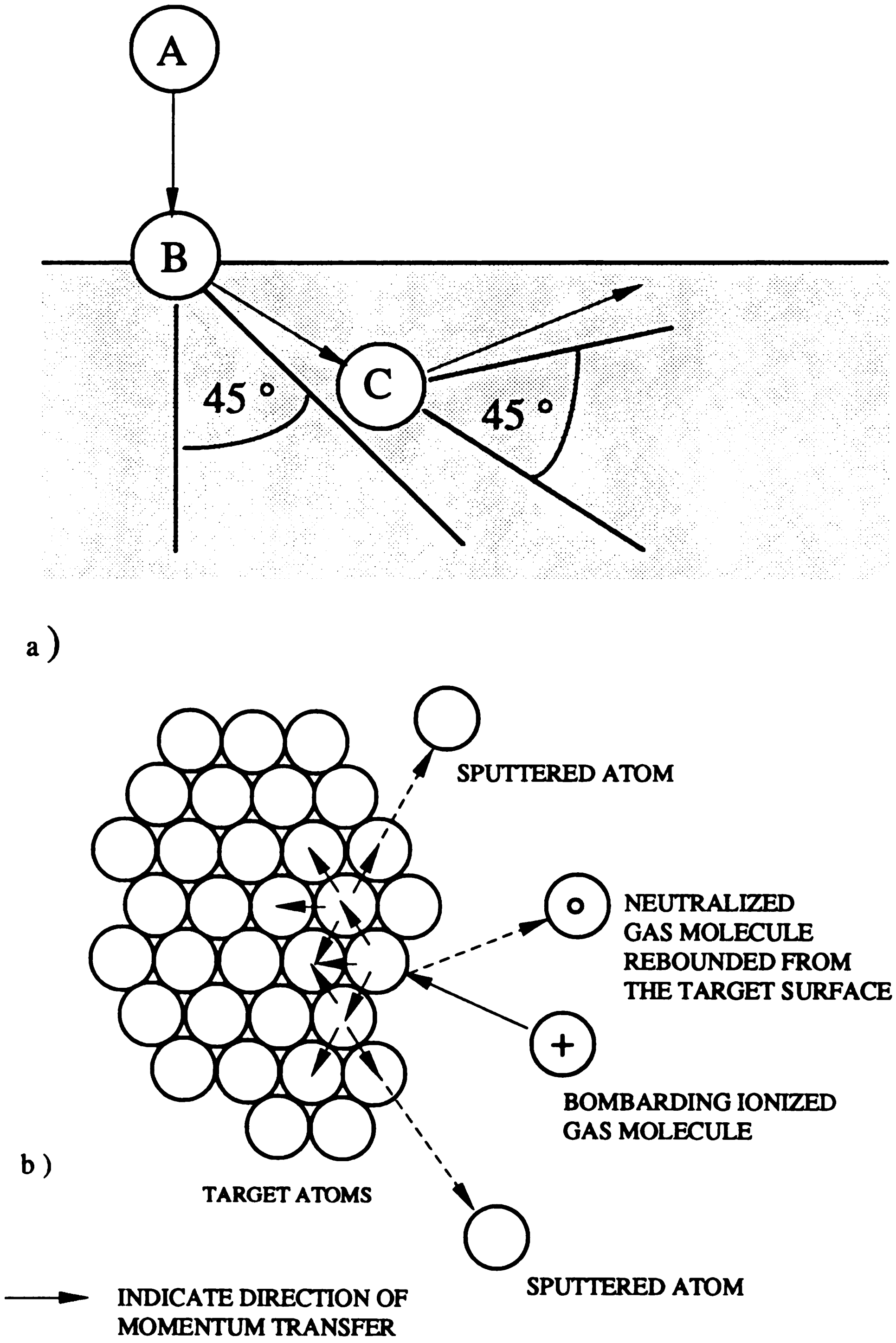

Figure 2-11 (a) Binary Collision Between Atom A and B, Followed by a Binary Collision Between Atom B and C. (b) Collision Process Responsible for Sputtering and Fast Neutral Generation [36]

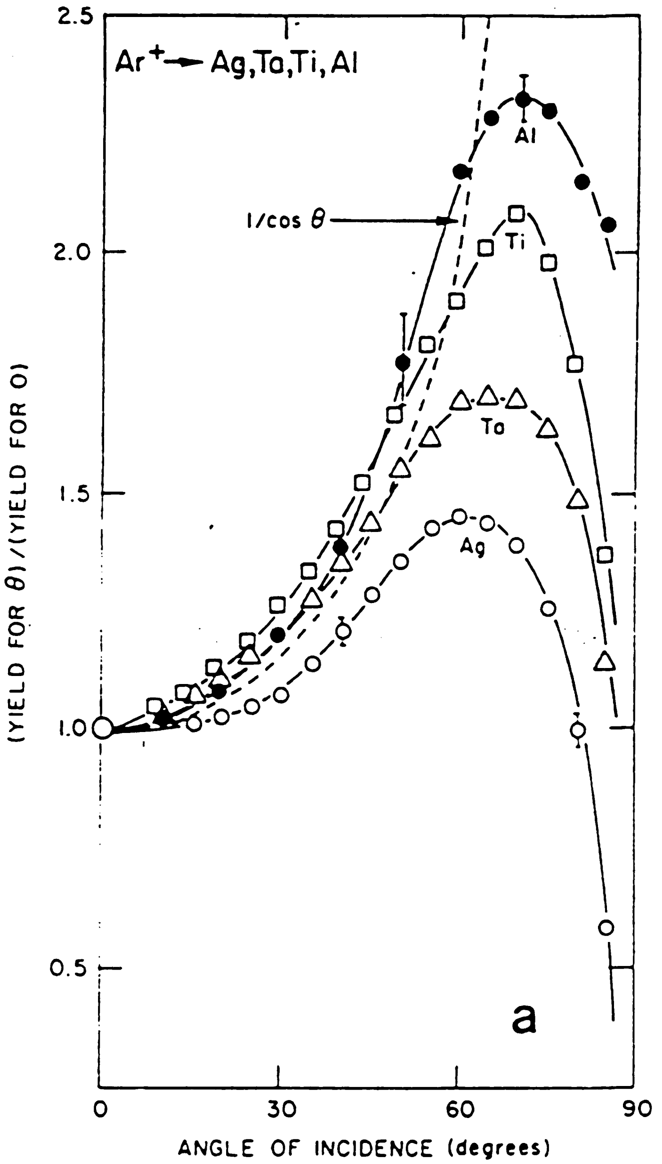

Figure 2-12 Variation of Sputtering Yield with Angle of Incidence for 1 keV Ar Ion Incident on Ag, Ta, Ti, and Al [37]

The sputtering yield also depends on a number of factors besides the direction of incidence of the ions; it depends also on the target materials, the target composition and structure, the mass of bombarding ions, and their energy. There is a minimum energy threshold for sputtering every material, as shown in Table 2-1. In the energy range of sputtering (10-5000 eV), the yield increases with ion energy and mass. Figure 2-13 [27] shows the sputtering yields of nickel as a function of energy for various noble gas ions. The sputtering yields of various materials in argon, at different energies, is given in Table 2-3 [36].

Table 2-3 Sputtering Yield for Metals in Argon (atoms/ion) [36]

Target	100 eV	300 eV	600 eV	1000 eV	2000 eV
Al	0.11	0.65	1.2	1.9	2.0
Au	0.32	1.65	2.8	3.6	5.6
Cu	0.5	1.6	2.3	3.2	4.3
Ni	0.28	0.95	1.5	2.1	
Pt	0.2	0.75	1.6		
Si	0.07	0.31	0.5	0.6	0.9
Ta	0.1	0.4	0.6	0.9	
Ti	0.08	0.33	0.41	0.7	
W	0.12	0.41	0.75		

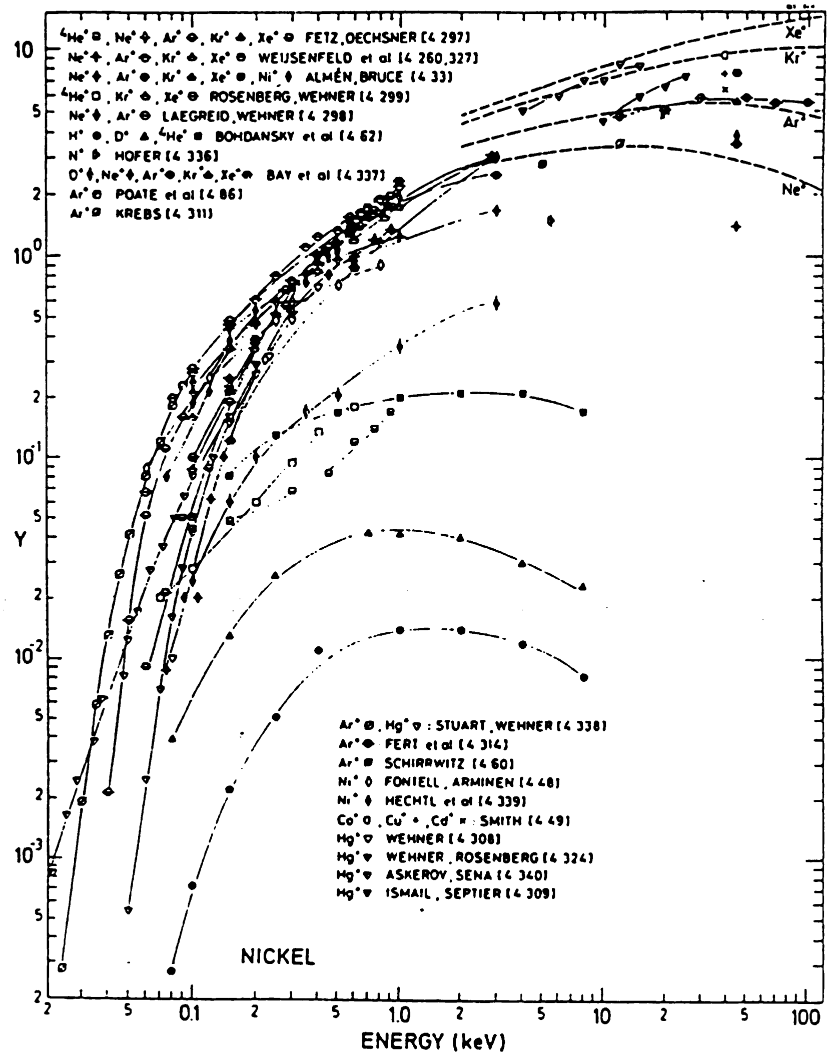

Figure 2-13 Sputtering Yield of Nickel as a Function of Ion Energy and Ion Mass [27]

Several matters related to sputtering yield should be noted. First, although the sputtering yields of various materials are different, as a group they are much closer in value to one another than the vapor pressure of comparable materials. This makes the deposition of multilayer films or multi-components films much more controllable by sputtering than by evaporation. Second, since the bombarding ions are not monoenergetic in glow discharge sputtering, it is not necessarily valid to use the sputtering yield value for pure metals when alloys and compounds are being sputtered. Third, since the mass differences between components, the momentum and energy will be distributed differently to each constituent resulting in different ejection probabilities for the atoms. Note that the sputtering yield ratio between the alloy components doesn't equal to the deposited materials composition ratio since there are many other factors will change the final composition outcome. This will be discussed in section 4.1. The tabulations of sputtering yields, however, are useful for obtaining rough indications of deposition of various materials.

For the deposition process, argon was chosen as the sputtering gas for its inert properties and low cost. The pressure range of operation is set by the requirements of the glow discharge (lower limit) and the scattering of sputtered atoms by sputtering gas (upper limit). Generally speaking, the higher the current at the cathode, the higher is the deposition rate (since more ions are striking the cathode, and thus are causing more sputtering).

In fact, sputtering is a highly inefficient process. About ~ 70% of the energy consumed during the sputtering process is dissipated as heat in the target, and ~ 25% by emission of secondary electrons and photons by the target. The target heating can raise target temperatures to levels capable of damaging the target, associated vacuum component and the backing electrode. Cooling of the target with water is typically used to maintain low target temperatures.

2.4.3 Sputter Deposition Film Growth

Upon being ejected from the target surface, sputtered atoms have energies about 10 to 40 eV. In general, the target-to-substrate spacings are 5-10 cm. The mean free path, λ, of a sputter gas atom under typical sputter pressure is 1 cm for Ar atoms at 0.6 Pa, less than 5-10 cm. (The mean free path is calculated from equation $\lambda = \frac{1}{\sqrt{2}\pi d_1 d_2 n}$, where n is the gas concentration, d_1 and d_2 are the atomic diameters of colliding atoms, one of them being the background gas atom's [34]). Thus, it is likely that the sputtered atoms will suffer collisions with the sputter gas atoms before reaching the substrate. The sputtered atoms may therefore arrive at the substrate with reduced energy and increased energy spread; be backscattered to the target or the chamber walls; or lose enough energy so that they are transported by diffusion in the same manner as neutral sputter gas atoms [34, 35]. As these events occur during the transport of sputtered atoms to the substrate, sputtering gas pressure can alter the energy of arriving matter and thus affect the properties of the deposited films.

The formation and growth of thin films on the substrate follows mechanisms of nucleation and growth, as shown in Figure 2-14 [38]. Atoms transfer the normal component of their velocity to the substrate and attach to the surface. After becoming attached to the surface, they are referred to as "adatoms". Adatoms may continue to move along the surface due to the kinetic energy associated with their initial lateral velocity, or by thermal activation from the surface. In some cases, the adatoms may re-evaporate from the surface into the vapor phase. As the adatoms migrate along the surface, they may interact with each other to form nuclei. In the formation process, the film passes through stages of nucleation → growth → island formation → island coalescence → continuous film formation.

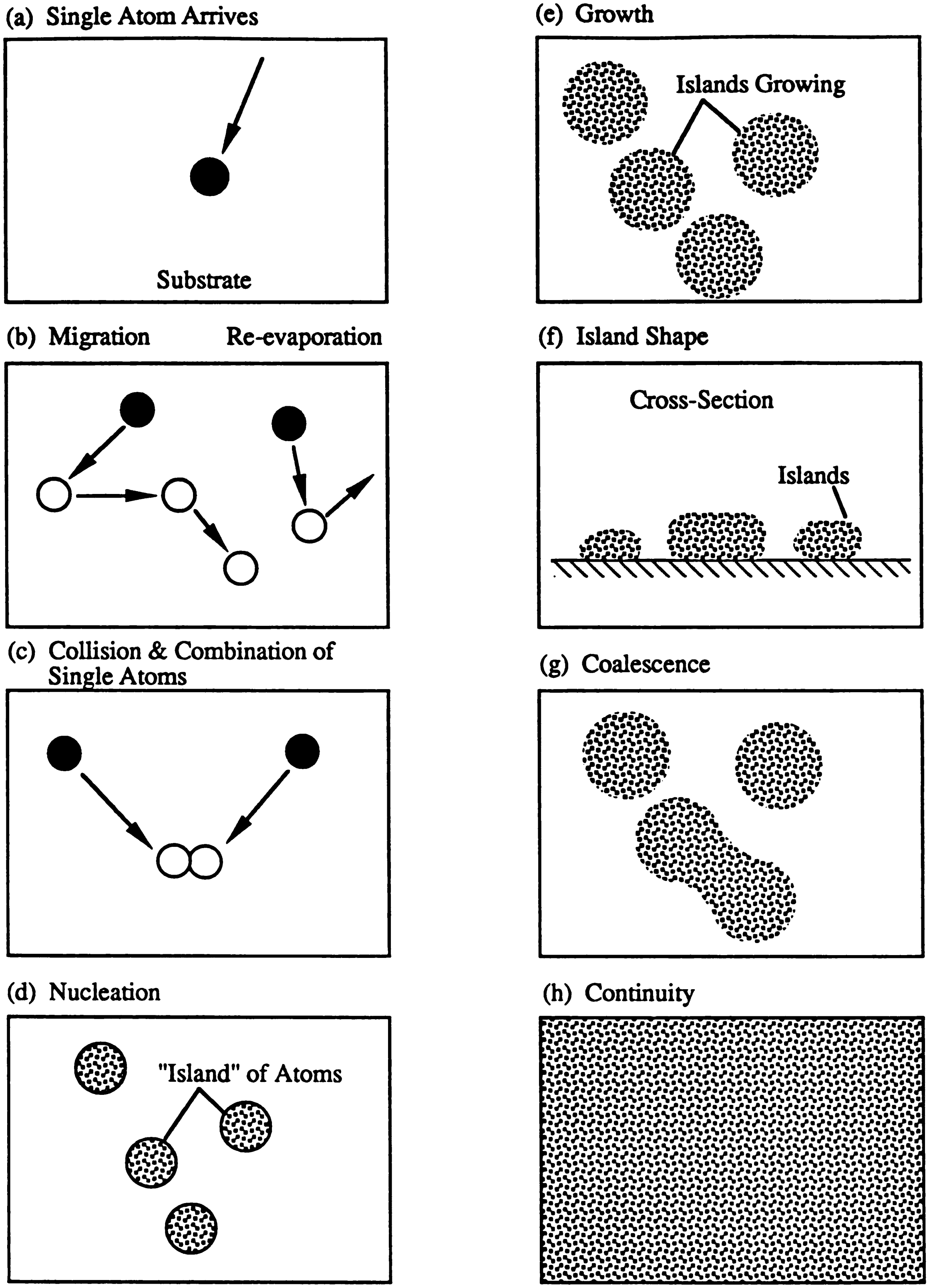

(a) Single Atom Arrives

(b) Migration Re-evaporation

(c) Collision & Combination of Single Atoms

(d) Nucleation

(e) Growth

(f) Island Shape

(g) Coalescence

(h) Continuity

Figure 2-14 Formation of Thin Film [38]

The substrate on which we desire to deposit a film is important in determining the quality of the films. Some factors influencing quality are the substrate's temperature, chemical nature, crystallographic structure and condition of the surface. Also, the substrate is subjected to impingement by many species during this process, as shown in Figure 2-15 [34]. The most important species are: 1) fast neutral sputter gas atoms (Ar), which retain significant energy after having struck and recoiled from the cathode. As they impinge upon the substrate, some may embed themselves in the growing film. 2) Negative ions are formed near the cathode surface by the reaction of secondary electrons. The latter can acquire substantial energy from Crookes dark space electric field, and thus also strike the substrate with appreciable energy. 3) High energy electrons, which are accelerated across the Crookes dark space, and then impinge on the substrate, and: 4) Low energy neutral sputter gas atoms (Ar), which strike the substrate at a high flux. However, the sticking coefficient of low energy neutral Ar atoms is negligibly small, and thus the only incorporation of Ar atoms into the growing film arises from fast neutral embedment. Finally, 5), contaminants present in the form of residual gases in the chamber can be incorporated into the growing film.

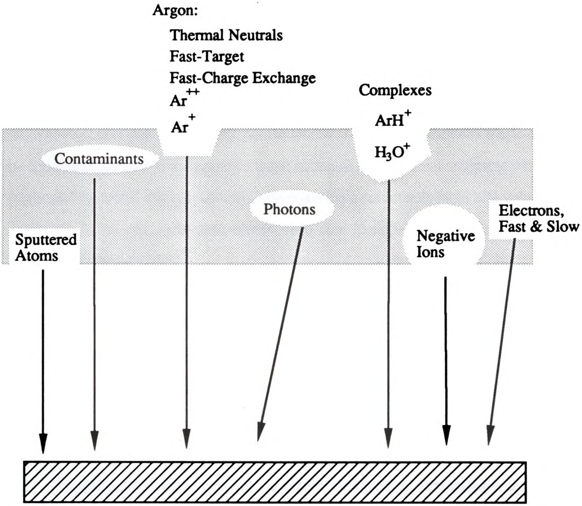

Figure 2-15 Particles Bombarding the Substrate in Sputter-Deposition [34]

2.4.4 Magnetron Sputtering

In general, the diode configuration is the simplest glow-discharge based sputtering system and possesses severe limitations that make it unsuitable for most practical applications. As a consequence, radio-frequency (rf) sputtering, and magnetron sputtering, are most often used to deposit thin films. The rf sputtering method is used for the deposition of insulator materials since the glow-discharge cannot be maintained with a dc voltage if the electrodes are covered with insulating layers. Also, it can be used to deposit conductive materials. The most common type of rf magnetron configuration uses the chamber and other grounded fixtures for the second rf electrode. With this single-ended configuration, the area of the sputtered target surface is usually small compared with that of the ground electrode, and only the target electrode has a sufficiently large bias voltage for sputtering. If the length of the magnetron is less than 30 cm, rf sputtering is as easy to implement as dc sputtering.

In both dc and rf diode sputtering, most secondary electrons emitted from the target do not cause ionization events with Ar atoms. They end up being collected by the anode or at substrates where they may result in unwanted heating. The application of a magnetron increases the ionization efficiency of elements by utilizing magnetic fields to help confine the electrons near the target surface and lengthen their paths by confining them to spiral orbits.

To describe the principle of the magnetron configuration, first consider the motion of an electron, mass m_e, and initial velocity v, that is perpendicular to a uniform magnetic field, as shown in Figure 2-16a [34]. The electron experiences a force, $F = qv \times B$, which is perpendicular to both its velocity and the direction of B. If no other forces are exerted on this electron, it will continuously be acted upon by the force F, and this will induce a circular motion with radius:

$$r = (m_e v / eB)$$

Comparing electrons and Ar^+ ions under equivalent conditions of B and particle energy, the equation for *r* shows that the Ar^+ ions have motion radii which are about 300 times larger than the electrons' due to the significant difference between their masses. This illustrates that the direction of electron motion in magnetron discharges is strongly influenced by the magnetic field, while the magnetic field does not significantly change the direction of Ar^+ ions as they cross the dark space.

Let there be a magnetic field, B, parallel to the surface and an electric-field ξ perpendicular to the surface, as shown in Figure 2-16b. Let the electric field ξ decrease linearly across the dark space of thickness L with ξ_0 at the surface of target. If *y* is the vertical distance above the target and the target surface is y = 0, then the magnitude of the electric field is given by:

$$\xi = \xi_0 (1 - y / L)$$

Assume the electron is initially at rest. Now the electron will be accelerated away from the target in a direction perpendicular to the surface by the electric field, but simultaneously it will experience a force due to the magnetic field, $F = qv \times B$. The electron velocity will therefore be altered from a direction perpendicular to the surface. If the magnetic field is strong enough to deflect the electron velocity so that it begins to return to the target surface before it leaves the magnetic field, its motion will be roughly cycloid as shown in Figure 2-16b. That is, as it approaches the target surface after having been deflected, the electron will be decelerated by the electric field, and eventually will come to rest (momentarily) at the target surface. At this point, the next period of the cycloid motion will be initiated, as it is once again repelled by the electric field. The maximum excursion of the electron from the target during such motion is given by [39]

$$y_{max} = \frac{1}{B}\left[\frac{2m_e}{e}(V - V_T)\right]^{1/2}$$

where V_T is the potential of target and V is the potential in the dark space at y_{max}.

The net result is that secondary electrons are trapped near the target surface by the combination of the magnetic and electric fields. Even though not every electron produces an ionization event, many more ions are generated than if the secondary electron escaped the discharge without the application of the magnetron.

In a planar magnetron [40], the target surface is planar, and the B-field is created by magnets behind the target, as shown in Figure 2-17 [34]. In examining these illustrations, it must be noted that the magnetic field lies parallel to the target surface half-way between the magnetron poles. In this region, the $E \times B$ field closes on itself. Thus, a continuous path for the "hopping" electrons is established. This region is called the "racetrack" and sputtering is very rapid in the racetrack portion of target. This will result in localized erosion of target, leading to loss of absolute planarity. In addition, since magnetrons are much more effective in causing secondary electrons to undergo ionization collisions, much higher currents occur for comparable voltage levels.

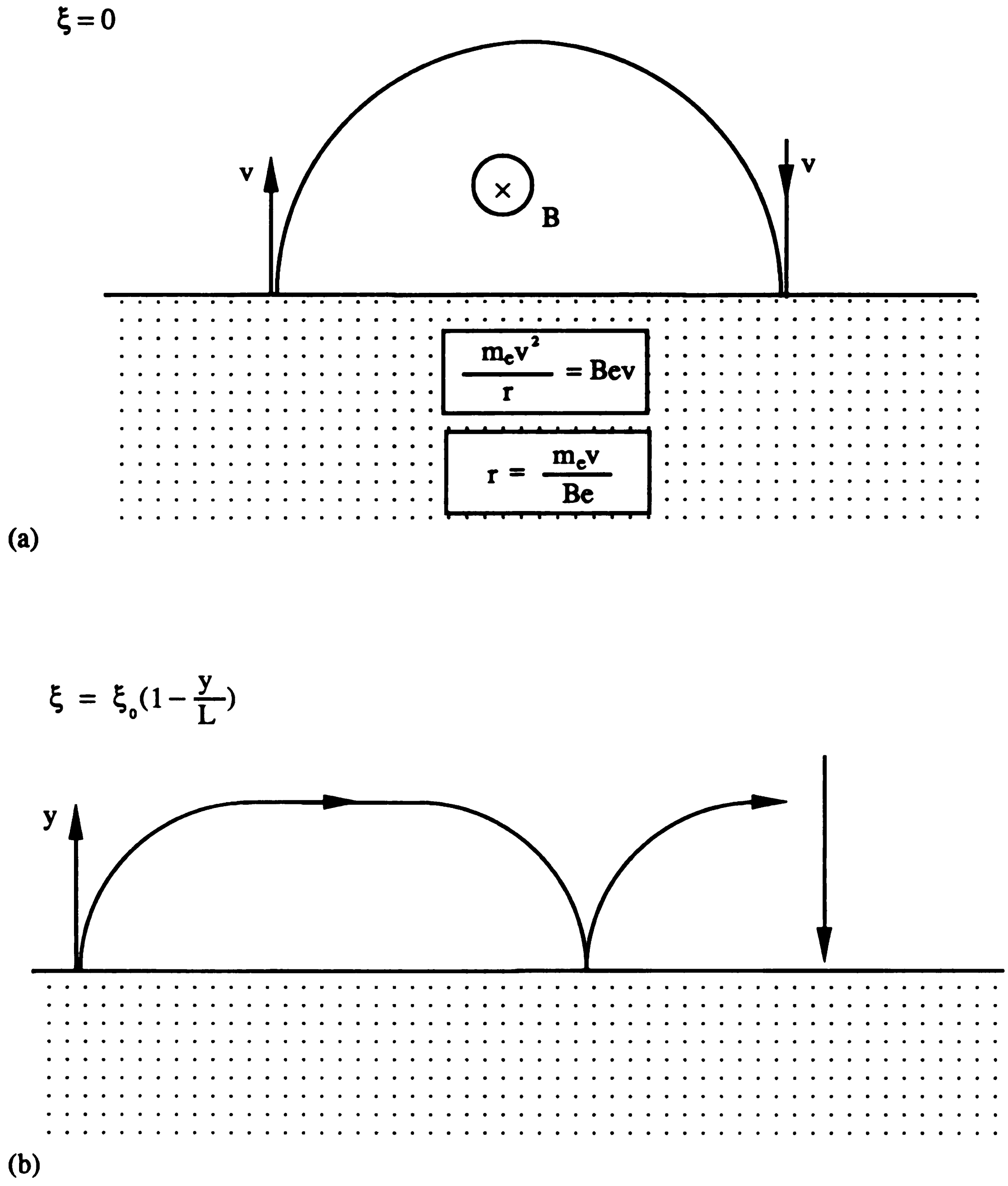

Figure 2-16 Motion of an Electron Ejected from a Surface with Velocity v into a Region of Magnetic Field B Parallel to the Surface [34]:
(a) with No Electric Field
(b) with a Linearly Decreasing Field

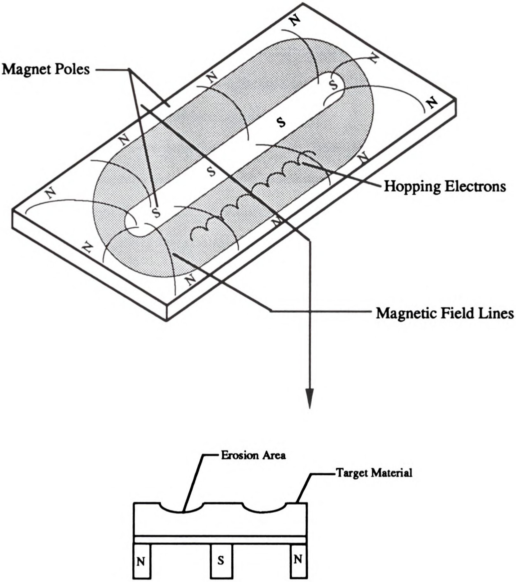

Figure 2-17 Schematic Drawing of Planar Magnetron Target and its Cross Section [34]

2.4.5. Deposition of Alloys Film

When an alloy surface is subjected to energetic particle bombardment, the different elemental components are not sputtered in proportion to their concentration in the alloy [34, 35, 41]. This phenomena is called preferential sputtering. The preferential removal of one component from the alloy surface results in the formation of an altered layer, which is a near-surface region with a composition different from the bulk alloy and depleted in the species experiencing the higher sputtering yield [41].

If a virgin target were used for sputtering, the layer of metal oxide will be removed. During this period, the removal of oxide will be accompanied by a change (usually decrease) of discharge current because of differing secondary electron coefficients for metal and oxide. After time, the nominal composition surface is exposed. Due to the preferential ejection of the high sputtering yield component, the sputtered flux leaving the surface would be different from the composition ratio of target. But, barring rapid diffusion in the target, this situation cannot last for long because the altered layer will become enriched with the low sputtering yield component. Ultimately, a steady-state can be set up, whereby elements are sputtered from the target surface in the same ratio as are present in the bulk target.

Note that the depletion of one component on the target surface will produce a concentration gradient of the components, and this will encourage diffusion. If diffusion happened during the process, steady-state can't be attained. At sufficiently low temperatures, the thermal diffusion can be minimized. So, it is very important to keep the target cold enough during the sputtering process.

Transport of the sputtered material from target to substrate is not merely a straight line travel. The collision between sputtered atoms and sputtering gas atoms will take place. Especially at high pressure, transport becomes more like a diffusion process. Also, as the mean free path of sputtered atoms decreases, more of them will land on other places inside the chamber and proportionately less on the substrate. Because of different mean free paths for different components, which depends on atomic radius, the ratio on the substrate is not expected to be the same as the flux leaving the target surface.

The next stage is the condensation of the vapor atoms on the substrate. The condensation coefficient is the proportion of the atoms that stays on the substrate without evaporation. This is determined by the arrival rate, temperature, and the bonding energy between substrate and adatoms. Usually, the condensation coefficient is different for each constituent causing an effective change in the composition of the depositing films.

In the glow discharge environment, the growing film will be bombarded by ions and to some extent there will be re-sputtering of the growing films. Since sputtering increases with increasing ion energy, such resputtering will be particularly effective for high energy sputtering. In addition, the films will be depleted of the component with the higher sputtering yield due to the resputtering.

Considering all of these various effects together, the composition of a sputter deposited alloy film can be different from that of the target. However, the composition change should be reproducible for a given set of process conditions. So by adjusting the process parameters, thin films with different compositions can be easily obtained.

2.5 Composition Analysis

In this study, the energy dispersive X-ray spectrometry (EDS) method was adopted to measure the composition. Because the necessary composition control in the deposition of TiNi thin films is to between one tenth and one hundredth of an atomic percent, the accuracy of composition measurement thus becomes very important. In this section, the principle of EDS analysis and the so called ZAF correction (See section 2.5.3) are thoroughly discussed. In order to obtain an accurate compositional result of thin film without interfering by the substrate, there is a criterion for the thickness, about 3 μm.

2.5.1 Principle of EDS Analysis

The scanning electron microscope-electron probe microanalyzer has been used to determine the compositions of thin films. As atoms are excited by electron beams, characteristic X-rays are emitted when an electron jumps from one shell to another of a lower energy state. By measurement of the energy or wavelength and number of X-rays emitted by emission or fluorescence spectrometry, compositional information in terms of the atomic species present can be obtained. Presently, the emitted X-rays are measured with an energy dispersive X-ray spectrometer (EDS) [42, 43, 44].

The relationship between the intensity of an X-ray line and the concentration of the element concerned is very complex. Information about the system's geometry, the behavior of the specimen and its constituent elements are necessary. Thus, complex mathematics and statistics must be applied to transform the X-ray raw data into the quantitative results.

As shown in Figure 2-18 [45], the electrons' distribution and the activated volume in thick and thin specimens are different. With thin specimens, X-rays can usually be regarded as having come from an area the size of the incident electron beam diameter. With thick, bulk specimens, determine this area of origin is much more complicated because electrons interact with a larger volume of the specimen. This interaction volume depends on several variables, such as energy of incident electrons, materials, and tilt angle. Thus, bulk samples will produce much larger error in quantitative work than thin specimens.

The most important technique for analyzing quantitative electron-excited results is known as a ZAF calculation. ZAF is an acronym for the three effects: atomic number (Z), absorption (A) and fluorescence (F). Noting that the Z correction is a combination of the 'stopping power' and the backscattering correction, both of which are primarily dependent on atomic number. After ZAF corrections, the specimen/standard intensity ratio can be converted into concentration.

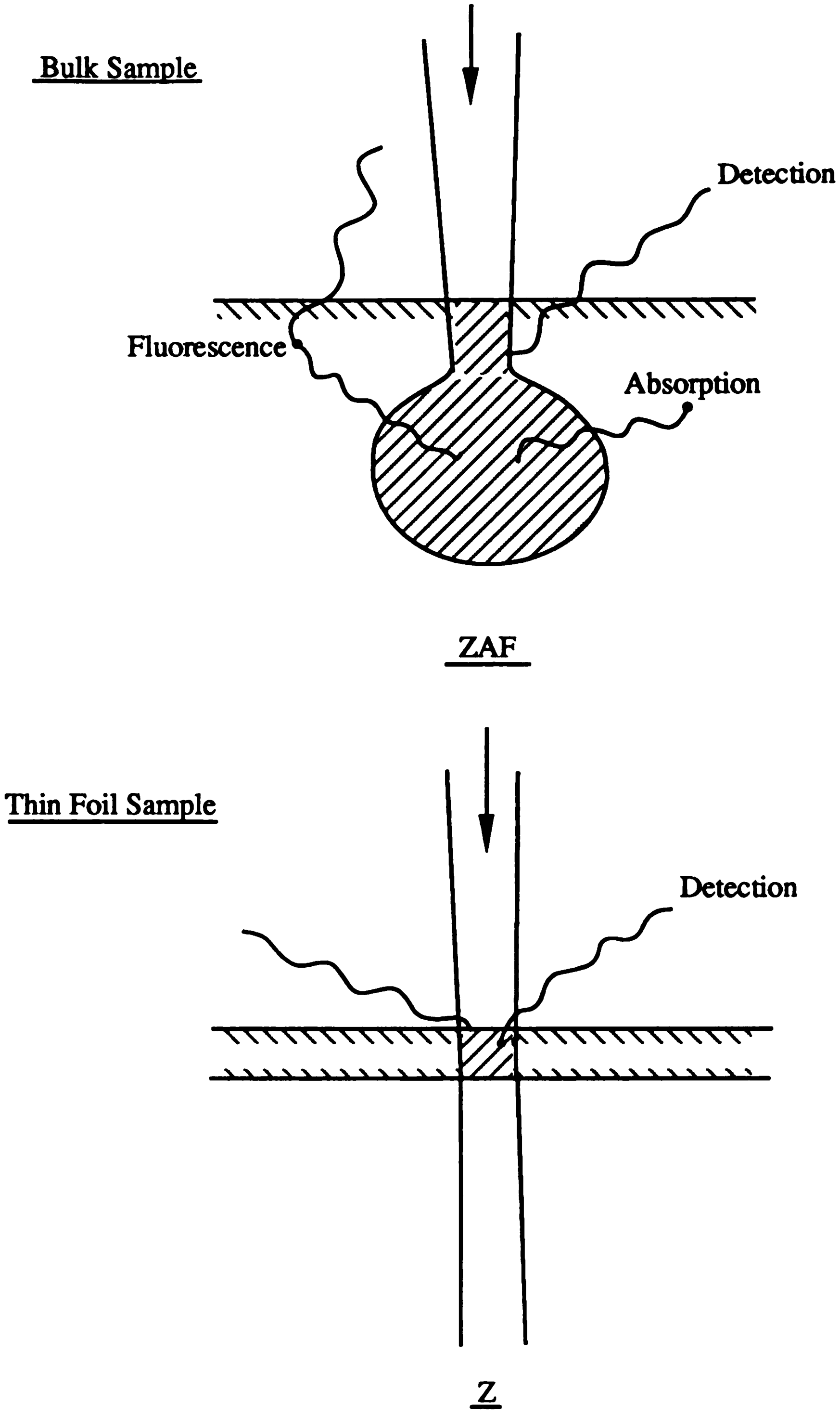

Figure 2-18 Schematic Distribution of Electrons and Activated Volume in a Thick and Thin Specimen [45]

2.5.2 Characteristic X-ray Intensity

The number of ionization (*dn*) per increment of electron path length (*dx*) on a pure element is

$$dn = Q_k \frac{N\rho}{A} dx$$

where Q_k is the ionization cross-section of the shell concerned (usually the shell K), N is Avogadro's number (6.02×10^{23}), ρ is the density, and A is the atomic weight of the element concerned. Assuming that incident electrons lose energy continuously along their path, there is a relationship between path length, x, and energy, E. By integration, the total number of ionizations produced along the trajectory of an electron with initial energy E_0 is :

$$n = -\int_{E_c}^{E_0} Q_k \frac{N\rho}{A} \frac{dx}{dE} dE$$

where E_c is the threshold excitation energy. The minus sign considers the decrease in E with x that makes dx/dE negative.

Defining the "stopping power" (*S*) of the bombarded material as $-dE / d(\rho x)$, then

$$n = \frac{N}{A} \cdot \int_{E_c}^{E_0} \frac{Q_k}{S} dE$$

multiply n by R (a factor taking into account the loss of ionization caused by electron backscattering) and ω_k (fluorescence yield, the fraction of ionization of K shell that result in characteristic X-ray emission) gives the characteristic X-ray intensity per incident electron on pure material

$$I_k = \frac{N\omega_k Q_k}{A} \int_{E_C}^{E_0} \frac{R}{S} dE$$

where ω_k is a constant, Q_k is a function of E_0 and E_c only.

2.5.3 ZAF Correction

If compounds were considered, the term $N\rho/A$ (the total number of atoms per unit volume in pure element) must be replaced by $CN\rho/A$ (the number of atoms of the element concerned per unit volume in the compound), where C is the concentration of that material. The ratio of characteristic X-ray intensity (I) from the specimen to that emitted by a standard (I_0) containing a concentration C_0 of the element concerned is given by:

$$\frac{I}{I_0} = \frac{\frac{CN\omega_k Q_k}{A}\left(\int_{E_c}^{E_0} \frac{R}{S}\,dE\right) \times F^a \times F^f}{\frac{C_0 N\omega_k Q_k}{A}\left(\int_{E_c}^{E_0} \frac{R_0}{S_0}\,dE\right) \times F_0^a \times F_0^f}$$

$$\Rightarrow \qquad C = C_0\left(\frac{I}{I_0}\right) \times (ZAF)$$

where $$(ZAF) = \frac{\left(\int_{E_c}^{E_0} \frac{R_0}{S_0}\,dE\right) \times F_0^a \times F_0^f}{\left(\int_{E_c}^{E_0} \frac{R}{S}\,dE\right) \times F^a \times F^f}$$

F^a and F^f are factors of absorption and fluorescence for specimen.
F_0^a and F_0^f are factors of absorption and fluorescence for standard sample.

(ZAF) can be separated into three correction factors which represent effects by atomic number, absorption and secondary fluorescence.

Z (atomic number) Factor Correction The Z factor term is a combination of S (stopping power) and R (backscattering). From Bethe's law S is represented by [46]:

$$S = -7.85 \times 10^4 (Z / A)(1 / E) \ln(1.166E / J)$$

where J is the mean ionization potential of element concerned. Thus, S is a function of electron energy E and atomic number. R represents the fraction of the incident electrons' energy remaining in the sample without loss by backscattering that can produce ionization. From Russ's proposal [47]:

$$R = e^{-0.04}Z(U-1)^{0.3}$$

where U is the overvoltage ratio (defined as E/E_c, E_c is critical excitation energy)

Thus, R is a function of Z and U. With both S and R calculable, the total Z term becomes the integral of (R_0/S_0) for standard divided by the integral of R/S for the unknown matrix.

A (absorption) Factor Correction Whenever X-rays pass through anything, they are absorbed according to Beer's Law [43]

$$I_f = I_i e^{-\mu\rho x}$$

where I_f is the intensity left, I_i is the initial intensity, ρ is the density and x is the distance, and μ is the 'mass absorption coefficient'.

As shown in Figure 2-19 [43], the distance traveled in the specimen by X-rays generated at a depth z is $z \times cosec(\theta)$, where θ is the X-ray take off angle. Therefore, the factor by which the X-ray intensity is reduced is $e^{-\mu\,cosec\theta\rho z}$. Hence, defining $\phi(\rho z)$ as a function of the depth distribution of X-ray generation, the total absorption factor is an integral:

$$F(\chi) = \int_0^\infty \phi(\rho z) e^{-\chi\rho z} d(\rho z)$$

where $\chi = \mu\mathrm{cosec}\theta$

$$F^a = \mathrm{F}(\chi)$$

Then the total A term correction is just $F(\chi)$ for the standard divided by $F(\chi)$ for the element concerned in the matrix.

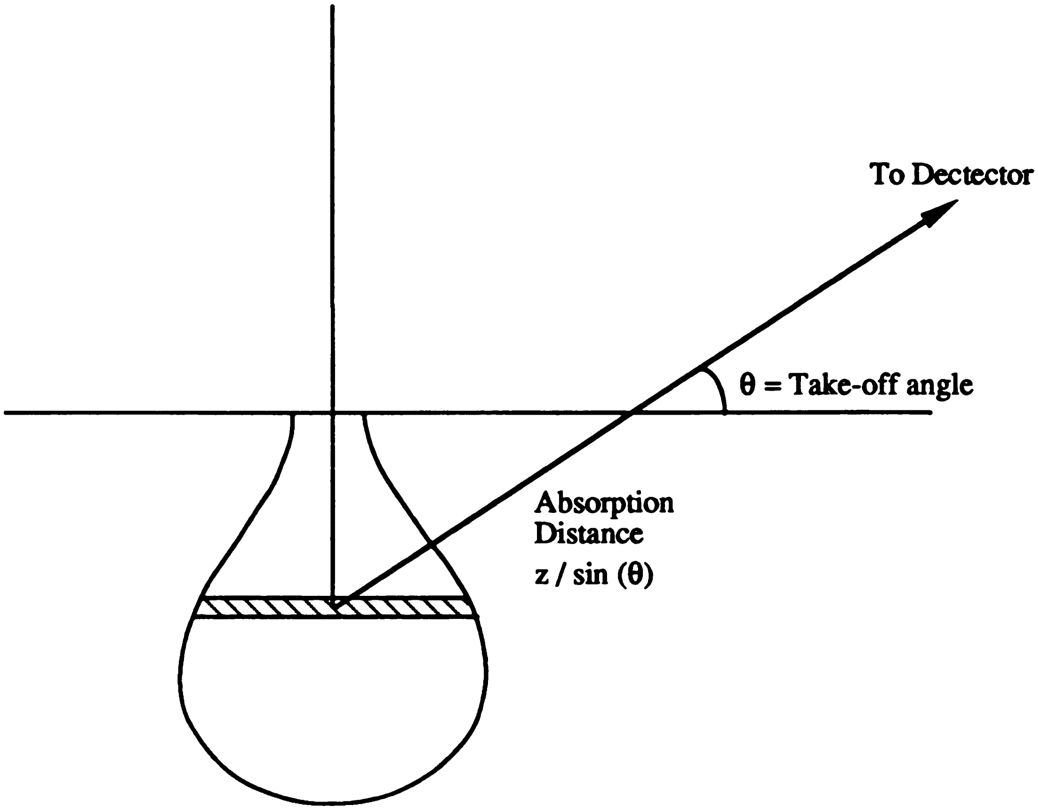

Figure 2-19 Schematic Diagram of X-Ray Generation in Sample and the Absorption of Photons from Each Depth z Enrout to the Detector, Depending on the X-Ray Take-Off Angle θ [43]

F (fluorescence) Factor Correction In binary systems, element A can be excited by characteristic fluorescence emitted by element B in the matrix, which will add to the intensity from element A produced by direct electron beam excitation. This process is called secondary fluorescence and a fluorescence correction is needed.

A correction for the additional fluorescence intensity from element "*i*" due to radiation from element "*j*" has been developed by Reed [48]:

$$\frac{I_i^j}{I_i} = 0.5C_j\omega_j(\mu_i / \mu_{mtx})((r_i - 1)/r_i)(A_i / A_j)P_{ji}((U_j - 1)/(U_i - 1))^{5/3}$$

where I_i^j is the fluorescence intensity which is added to the primary intensity I_i, ω_j is the fluorescence yield for element j, r_i is the absorption jump ratio for element *i* (which is defined as the mass absorption coefficient on the high energy side divided by that on low energy side), μ_i is the mass absorption coefficient, μ_{mtx} is the matrix mass absorption coefficient which is a sum of the coefficient for each element in the matrix times the element's concentration, A_i and A_j are the atomic weights of element *i* and *j*, the *P* factor which is 1.0 for K-K and L-L fluorescence but is taken as 0.24 for K-L and 4.2 for L-K respectively, *U* is the overvoltage.

Therefore, the fluorescence correction is $(1 + \sum_{j \neq i} \frac{I_i^j}{I_i})$, or, 1 plus the sum of the fractional additional intensities produced by each individual element in the matrix. Note that there is no fluorescence in the pure standard, so no ratio to the pure standard is needed. Hence if we can calculate Z, A and F, the true concentration of the specimen can be determined.

But since every correction term depends in one way or another on the composition of the matrix, such as determining the sum terms of total stopping power, secondary fluorescence or mass absorption coefficients of the overall elements in the matrix, the concentrations in the samples must be approximately known in advance. This circular

process needs an iterative calculation, carried out by making a first approximation to concentration, computing Z, A and F, applying them to get better concentration values, re-computing the Z, A and F terms using this second approximation, and so on, until, a desired levels of accuracy is attained.

CHAPTER 3 EXPERIMENTAL METHODS

The principal goals of this work are to study the effect of the processing parameters, such as working pressure, voltage, power, and distance, on the composition in TiNi thin films prepared by the dc magnetron sputtering method. These experiments were undertaken to develop a better understanding of the factors affecting the composition shift between the target and the deposited films. This chapter describes the detailed procedures used to fabricate TiNi thin films and the characterization methods employed to study their composition and thickness.

3.1 Materials

The sputtering target alloy, with a composition of $Ni_{51.3}Ti_{48.7}$, was purchased from Special Metals Corporation in the form of a UDIMET® Nitinol bar, hot rolled and peeled, with $A_s = -14$ °C, $A_f = -10$ °C, 305 mm long and 76.2 mm in diameter. This binary alloy bar was then machined into round disks, 50.8 mm in diameter and 3 mm thick by EDM. The surfaces of these disks were then ground by 0.3 μm abrasive Al_2O_3 particles and used as targets for the TORUS®-2C dc magnetically enhanced sputtering cathode assembly.

1000-series aluminum alloy sheets were widely employed for parts in the fixture design, such as sputter shutter, sputter shielding, and substrate holder. After machining, these aluminum parts were first cleaned in an etchant, consisting of one part HF, three parts of HNO_3 and five parts H_2O by volume, followed by distilled water, acetone and methanol.

TiNi thin films were deposited upon microscope slides (76.2 mm × 25.4 mm). The slides were used as substrates in the sputtering processes because they facilitated the process of acquiring free-standing thin films for composition analysis.

3.2 Deposition Equipment

3.2.1 System Geometry

The sputtering processes were carried out in a vacuum system equipped with a single sputtering cathode, shown schematically in Figure 3-1. The source was mounted through a standard 25.4 mm hole on the side of vacuum chamber in a 152.4 mm knife-edge flange. Being in a vertical orientation, neither the substrate nor target can be contaminated by falling particles. The stem of the sputtering source was modified by mounting a threaded aluminum tube (254 mm long and 25.4 mm in diameter), and equipped with a port-sealing mechanism to prevent leaking on the original short threaded stem. By means of this modification, the processing distance between target and substrate could be directly adjusted from outside of the chamber without venting.

The sputter shielding with a window (102 mm × 51 mm) opened at the sputtering position, was fixed between sputter shutter and substrate holder. The shutter plate, whose vertical position was changed via the moving stage controlled by a rotary feedthrough on the backside of the chamber, was set at 25.4 mm in front of the substrate holder. The substrate holder allowed a maximum of five separately exposable substrates to be installed at one time. During deposition, the object substrate was moved to the position facing directly in front of the target by the other moving stage, and the distance between them was controlled by the movable stem on the sputtering source. Substrates other than the one to be processed were covered and protected from the sputtered flux by the sputter shielding.

The thickness monitor crystal (See Section 3.2.4) was set at a position directly behind the substrate to be processed. Intermittent deposition-rate measurements were made by temporarily lowering the object substrate to expose the oscillator crystal.

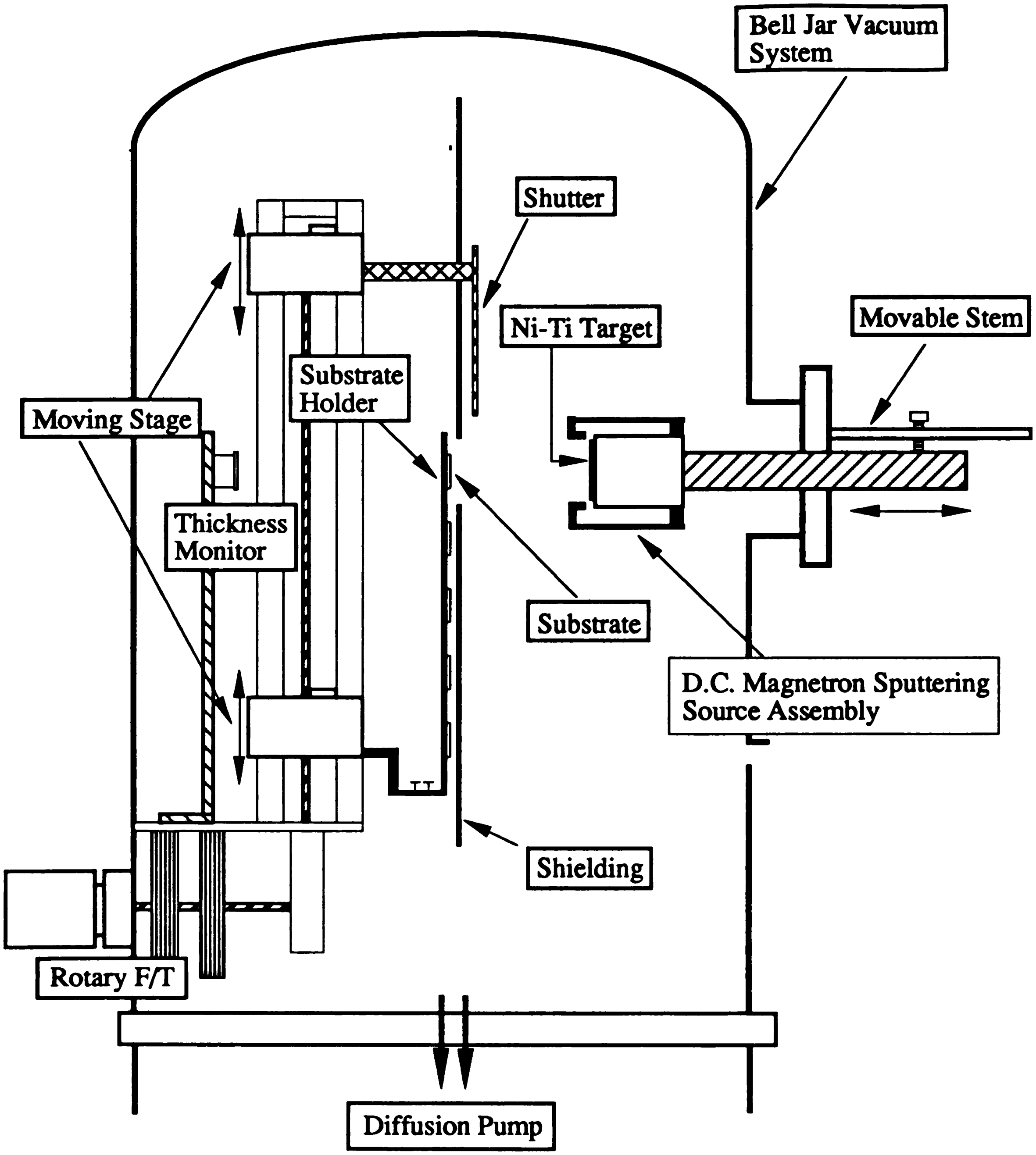

Figure 3-1 Schematic Diagram of D.C. Magnetron Sputtering System

3.2.2 Pumping System and Gas Pressure Monitors

The high-vacuum pumping system included one diffusion pump and one mechanical pump connected in series. The diffusion pump used for the vacuum system is a model HS-10 made from the Varian/Vacuum Company with a pumping speed of 4000 liters/second of air. A water-cooled trap was used. With the help of low-vapor-pressure silicone fluid (DC 705), the base-pressure was reach 8.5×10^{-4} Pa without baking the chamber. After baking for over 12 hours (using the flexible electric heating tapes wrapped around the chamber wall) and pumping down at least 24 hours, the ultimate base pressure reached 3×10^{-5} Pa with typical partial pressures: $P_{H_2O} = 1\times10^{-5}$ Pa, $P_{N_2} = 9\times10^{-6}$ Pa, and $P_{O_2} = 2\times10^{-6}$ Pa.

A Pirani Vacuum Gauge from Kurt J. Lesker Company was installed to read the higher range pressures from 0.1 to 10 Pa and to monitor the pressure during sputtering processes. An ion gauge was also installed to obtain the lower pressure values such as base pressure. Furthermore, a Dataquad quadrupole mass spectrometer from Spectramass Inc. was attached to the chamber to measure the partial pressure of residual gases. It also served as a high-vacuum gauge and a leak detector.

3.2.3 Sputtering Cathode assembly and Power Supply

The construction of the TORUS®-2C magnetron sputtering source is illustrated in Figure 3-2. Individual segments of the magnet are mounted between circular metallic pole-pieces and the whole is formed into one solid unit. The cooling water passes up through the magnet assembly, around its top surface immediately behind the solid copper mounting jacket where the target was secured by the retaining ring, and down again. Water also passes down around the outside of magnet assembly, then behind its base, and out the back.

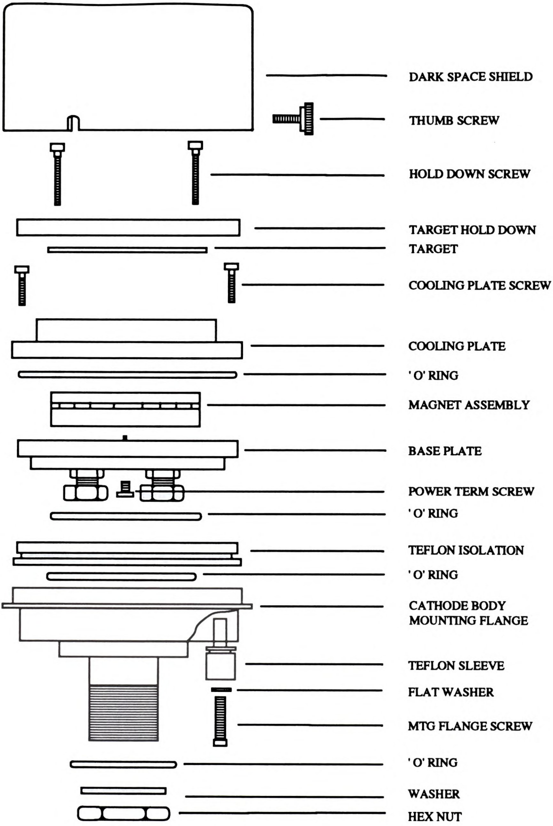

Figure 3-2 Exploded View of TORUS-2C Magnetron Sputtering Source.

The TORUS®-2C sputtering source design is based upon a modified Penning Discharge Principle. This design, with its powerful Samarium-cobalt magnets and shaped pole-pieces enhances the magnetic field immediately above the plane of the target. Instead of allowing secondary electrons that are emitted during sputtering processes to impinge upon the substrate, TORUS®-2C can capture electrons released near the target, concentrate them, and employ them to develop higher sputtering efficiency.

The power supply was a model Advanced Energy MDX1K. The unit will deliver 1 kW to a magnetron cathode at 1000 V and is controlled with any of three regulation modes: power, current or voltage.

3.2.4 Thickness Monitor

A quartz crystal thickness monitor (Leybold Inficon Inc. XTM/2 Deposition Monitor), consist of a quartz crystal sensor (Standard Sensor 750-207-G1) and a monitor/controller unit, was employed to measure deposition rate. The quartz crystal was fabricated into a disk with 12 mm in diameter, and had a 6.0 MHz resonant frequency. It was held right behind the substrate holder at the processing substrate position. Since measurements were intermittent, the quartz crystal sensor's water cooling system was not used.

In principle, the resonant frequency, f_q, of the quartz crystal sensor varies as a function of the mass of matter deposited on it [49]. As a result, the mass of film deposited can be expressed as

$$mf = \left(N_q \rho_q / \pi f_c Z\right)\{\tan^{-1}[Z \tan(\pi(f_q - f_c)/f_q)]\}$$

where N_q is the frequency constant for AT-cut quartz crystal, ρ_q is the density of quartz, f_q is the resonant frequency of uncoated quartz, f_c is the resonant frequency of coated quartz, and Z is the acoustic impedance ratio which is written as

$$Z = \left(\rho_q \mu_q / \rho_f \mu_f\right)^{1/2}$$

where ρ_f is the density of quartz crystal and deposited film, and μ_q and μ_f are shear moduli of quartz crystal and deposited film respectively. The deposited film thickness can be calculated from film mass and film density accordingly. In the present work, the density of alloy film is replaced by its bulk density of 6.5 gm/cm^3, and the shear modulus replaced by 2.48×10^{11} dyne/cm^2. The ρ_q and μ_q are obtained from manual 2.649 gm/cm^3 and 3.32×10^{11} dyne/cm^2. So, the Z factor is calculated to be 0.7386.

3.3 Deposition Procedure

3.3.1 Preparation

Substrate Cleaning All substrates were cleaned by acetone and methanol, respectively, in an ultrasonic cleaner for about 15 minutes to remove grease contamination prior to being installed. the substrate holder was polished by sand paper (grid No. 600) to remove previously deposited coatings, and then cleaned by distilled water, and subsequently by acetone and methanol.

Evacuation The vacuum chamber was evacuated by diffusion pumping for more than 24 hours after the pressure was brought down to 4 Pa by the mechanical pump. Electric heating tapes were used to bake out the adsorbed water vapor yielding the vacuum system base pressure below 3×10^{-5} Pa

Pressure Set Up The chamber was back-filled with argon gas and the Mass Flow Meter/Mass Flow Controller (from MKS Instruments Inc.) was used to control the chamber pressures in the region from 0.4 to 1.1 Pa. Detailed process conditions will be listed later.

Target Wear-In A $Ni_{51.3}Ti_{48.7}$ alloy target was used to deposit the films. During installation of the target, exposure to some physical handling and to atmospheric gases was unavoidable. Where the goal is to deposit films composed exclusively of the pure target material, target wear-in/clean up should be done prior to deposition on the substrate behind a sputter shutter. The virgin alloy target was pre-sputtered for 0.5 hour at higher power levels to attain steady-state sputtering conditions. This procedure removed oxides and contaminants and prepared it to produce high quality films. This preliminary wear-in also cause thermal expansion of the target which seats it properly in its cooling mount in preparation for later runs. Afterwards, the alloy target was pre-sputtered for 10 minutes under the experimental process condition at the beginning of each individual deposition run.

3.3.2 Processing

Condition Set Up There were five process factors considered in this study: target erosion, working pressure, cathode voltage, cathode power and working distance. For experimental convenience, only one variable was held constant per test. The detailed process conditions for every test run will be shown in section 4.2.

Deposition Rate Monitor At the beginning of each experiment run, the whole substrate holder was at a position lower than the processing position. After the target was pre-sputtered for at least 10 minutes under the desired process condition, the thickness monitor was exposed by raising the sputter shutter. Thus, the thickness monitor began to measure the deposition rate. Exposure of the sensor to the sputtering source was limited to one minute to avoid a temperature increase in the quartz crystal, however, the exact temperature of the quartz crystal was not known. The deposition rate was assumed to be constant during a run.

Film Deposition Prior to exposing the substrates to the sputtering source, the deposition rate was estimated by the thickness monitor, and the desired sputtering time was determined such that the total thickness of film was at least 3 μm allowing for the accurate measurement of composition. A series of substrates was set on the holder. One substrate was exposed per run. When the processing conditions stabilized, the target shutter was opened allowing for the deposition of thin film.

3.4 Composition Analysis

Elemental composition of the as-deposited films was determined by energy dispersive X-ray spectroscopy (EDS) microanalysis in a Hitachi S-2500 scanning electron microscope (SEM). This technique can determine the presence of various elements by analyzing the different energies of their characteristic X-rays, which are indirectly stimulated by incident electrons. Although the probe of incident electrons is very small, the area where X-rays are produced is much wider than the electron probe and reaches deeply into the sample. Films with thickness of at least 3 μm on glass substrates were illuminated by the electron beam with an energy of 20 keV. Since no Si characteristic radiation was observed, the substrate was taken to have no interaction with electrons, and the spectra could be then treated by a ZAF correction.

A program called ZAF-4, supplied by Link Analytical Inc., was used to analyze all the spectra, which were collected under carefully controlled conditions. The optics of the electron beam and the geometry between lens, sample and X-ray detector were rigorously kept consistent during data collection. The L_aB_6 electron source has to be stabilized for at least 0.5 hour prior to taking any spectra. All the spectra were collected at the same working distance (15 mm), magnification (2000 ×), tilting angle, dead time percentage and time interval.

The electrical parameters of the lens remained untouched throughout the whole process and the height of sample was adjusted to maintain a constant working distance. The Kα peak, acquired from a pure nickel standard and employed as a calibration spectrum, was collected every 15 to 20 minutes. Pure titanium and a $Ni_{49.9}Ti_{50.1}$ alloy were employed to be the standards for composition analysis, and the composition of target alloy was also measured simultaneously to evaluate the accuracy of this method. The bulk materials were last polished by using 0.05 μm alumina powder to yield mirror-like surfaces, and then cleaned by acetone and methanol. The specimens, including standards, were loaded on a graphite stage without tilting.

The composition of the sputter-target alloy determined by the ZAF method was: 50.59 at% Ni and 49.41 at% Ti. The results shows that the measured titanium content is about 0.7 at% higher than the manufacturer's specification, which was considered to be nominal.

3.5 Thickness Measurement

The thickness of the as-deposited films were also used to verify the measured deposition rate. To obtain a thickness profile, a Dektak II profilometer was employed to scan across a 3 mm wide step produced by masking the substrates during deposition. The profiling instrument draws a fine stylus along the surface containing the stepped film with speed 1.5 mm/min. Whenever the stylus encounters a step, a signal variation (based on differential capacitance) yields an indication of the step high. The information is displayed on a CRT.

CHAPTER 4 RESULTS AND DISCUSSION

During the deposition of alloy films, the various factors that would cause the composition of sputtered film to be different from that of the target alloy composition were generally described in section 2.4.5. In this study, TiNi thin films were fabricated by dc magnetron sputter-deposition under different process conditions. Actually, processing parameters were chosen in order to determine which factors mentioned above would dominate during the deposition process. Therefore, there are two major parts in this chapter. The first part concentrates on the discussion of how these factors can be applied to this study. Then, in the second part, the experimental results showing the effects of sputtering process parameters on the composition of sputtered films are presented and interpreted by means of the discussions reported in the first part.

4.1 Factors Determining The Composition of The Sputter-Deposited Thin Films

For metallic targets, the sputtering processes can be described by elastic collision in the surface layers of a solid. If an incident ion with sufficient energy collides with an atom of the solid, it creates a primary knockon atom. For the collision cascades started by this primary knockon atom, it is convenient to distinguish between three qualitatively different situations [50].

(1) The single-knockon regime. Recoil atoms from ion-target collisions receive sufficiently high energy to be sputtered, but not enough to generate recoil cascades.

(2) The linear cascade regime. Recoil atoms from ion-target collisions receive sufficiently high energy to generate recoil cascades. The density of recoil atoms is sufficiently low so that knock on collisions dominate and collisions between moving atoms are infrequent.

(3) The spike regime. The density of recoil atoms is so high that the majority of atoms within a certain volume are in motion.

Qualitatively, the single-knockon regime applies for ion bombardment at low energies, i.e. close to the sputtering threshold and for light ions, where mostly only small energies are transferred to target atoms. The linear cascade regime characterizes ions with medium to large atomic number in the keV energy region. The spike regime is reached for bombardment of large atomic mass targets with large mass ions or molecular ions at energies around 20 to 80 keV.

Since the planar magnetron source is usually operated in argon at a pressure of 0.15 to 1.5 Pa and at cathode potentials of 300-1000 V, under these conditions, the model for sputtering is limited to the linear cascade regime. However, there is no clear boundary between linear cascade regime and single-knockon regime, and the single-knockon model will be invoked as necessary.

4.1.1 Preferential Sputtering And Component Sputtering Yield Ratio

Due to preferential sputtering in the sputtering of alloy materials, the preferential removal of one component from the surface leads to the formation of the so-called "altered layer", which is a near-surface region with composition different from the bulk composition. At sufficiently low temperatures, when thermal diffusion is not important, the altered layer stays at a finite thickness and steady-state conditions can be reached where the amount of material sputtered from each species becomes proportional to the bulk concentration.

At steady-state, the ratio of the number of sputtered atoms n_A of component A to n_B of component B must be equal to the ratio of the bulk concentrations c_A / c_B [41]

$$n_A / n_B = c_A / c_B \qquad (4.1)$$

Since the ratio of the number of sputtered atoms n_A / n_B is equal to the ratio of the product of component sputtering yield Y_i and equilibrium surface concentration c_i^s of component i during sputtering, then

$$c_A / c_B = n_A / n_B = Y_A \cdot c_A^s / Y_B \cdot c_B^s$$

$$\Rightarrow \qquad \frac{Y_A}{Y_B} = \frac{c_A / c_B}{c_A^s / c_B^s} \qquad (4.2)$$

Equation (4.2) allows the experimental determination of the ratio of the component sputtering yields by measuring the surface and as well as the bulk composition, i.e. the changes in surface composition under ion bombardment. In addition, the component sputtering yields can be compared to the yields of the pure elements. Generally, the sputtering yields for the alloy target components are different from those of the pure elements.

Based on Equation (4.2), systematic studies on alloy composition were performed on a number of binary alloy systems [41]. The experimental results showed that the observed surface enrichment is mostly in agreement with the sputtering yields of the pure elements, i.e. the component with the lower elemental yield becomes enriched under ion bombardment.

Different models have been proposed to predict the changes in surface composition, such as mass effects and surface binding effects [50, 51, 52]. The mass effects model predicts that the depletion of the lighter target component and it becomes prevalent with decreasing energy. The surface binding energy argument predicts the enrichment of the component with the higher surface binding energy or heat of atomization. The different effects can give opposite results and generally a combination of these two effects will occur. However, it was found that enrichment after the treatment of mass effects and surface binding effects is in most cases too small as compared to the experimentally observed changes [52].

In the case of TiNi alloy system, properties comparison between the nickel and titanium of atomic mass, atomic radius, heat of atomization, sputtering threshold energy, and the sputtering yields at 600 eV is indicated in Table 4-1.

Table 4-1 Properties Comparison of Titanium and Nickel

	Titanium	Nickel
Atomic Mass	47.90	58.71
Atomic Radius	1.46 Å	1.25 Å
Heat of Atomization	473 KJ/mole	429 KJ/mole
Sputtering Threshold Energy	20 eV	21 eV
Sputtering Yield (at 600 eV)	0.41 atoms/ion	1.5 atoms/ion

Since pure elemental Ni has a higher sputtering yield than pure elemental Ti under the same ion bombardment energy, it is believed that $Y_{Ni} > Y_{Ti}$ is still true in the sputtering of TiNi alloys. From the mass effects model [50], the component with lighter mass and lower threshold energy is in favor of being preferentially sputtered and becomes more prevalent with decreasing energy. This means that the sputtering yield ratio Y_{Ni}/ Y_{Ti} will decrease as the energy decreases.

The component sputtering yield ratios in the magnetron sputter-deposited TiNi amorphous thin films were studied by Chang using IBAD method [26]. The experimental results showed $Y_{Ti} > Y_{Ni}$ and the ratio of Y_{Ti}/ Y_{Ni} (note inverse ratio) increased from 1.75 at 500 eV to 9 at 50 eV. The trend for the changes of component sputtering yield ratios is the same as that for crystallized alloys, and can be explained using the same mechanism. However, $Y_{Ti} > Y_{Ni}$ in the amorphous alloy is opposite to the assumption of $Y_{Ni} > Y_{Ti}$ in the crystalline alloy. This phenomenon could be understood considering the surface binding energy effects. For a crystalline binary alloy AB, the surface binding energies U_A and U_B have been expressed by Kelly [52] as functions of the nearest-neighbor bond strengths U_{AA}, U_{BB} and U_{AB}. Thus, one obtains for U_A and U_B:

$$U_A = -C_A^S Z_S U_{AA} - C_B^S Z_S U_{AB} \qquad (4.3)$$

$$U_B = -C_B^s Z_s U_{BB} - C_A^s Z_s U_{AB} \qquad (4.4)$$

where Z_s is the surface coordination number, and c_i^s is the equilibrium surface concentration of component *i* during sputtering. As for amorphous alloys, the structures almost have a complete lack of periodicity and there are no specific distinctions between U_{AA}, U_{BB} and U_{AB}. All bond strengths can be assumed identical in the amorphous alloy. Therefore, there are no differences between U_A and U_B, and the mass effects dominate the preferential sputtering. This will cause the depletion of Ti component in the amorphous TiNi alloy during sputtering. Because the as-deposited TiNi thin films are in amorphous form, Ni-enrichment thin films are predicted due to the preferential resputtering of Ti component.

4.1.2 Angular Distribution of Sputtered Atoms

In the case of sputtering by linear cascades the ejection distribution from a polycrystalline solid is largely independent of mass, energy and incident angle of the bombardment ions [53, 54]. The ejection distribution is rotationally symmetric with respect to the surface normal and conforms to [54]

$$\frac{dY}{d\Omega} \approx \cos^{\nu_e} \theta_e \qquad 1 \leq \nu_e < 2 \qquad (4.5)$$

where *Y* is sputtering yield, *Ω* is the direction of emission, and θ_e is the polar angle of the emitted particle. A more or less pronounced "over cosine" distribution ($\nu_e > 1$) is often observed [55]. Such behavior is expected from the mechanism of linear cascades and is reproduced by computer simulation [56].

In the low-energy regime of medium to heavy ion sputtering, i.e. $m > 4$ and $E < 1$ keV, the emission distribution depends on the incident angle, and deviates from the cosine law giving higher emission at larger polar angles. These so called "under-cosine" distributions are generally explained as a result of shallow cascades, where too few collisions are available to acquire momentum randomization [53].

Then, if an alloy is sputtered, the angular distribution of the sputtered atoms can be different for each component. Basically, they are all assumed to follow the cosine law distribution but have different shapes, as shown in Figure 4-1 [57].

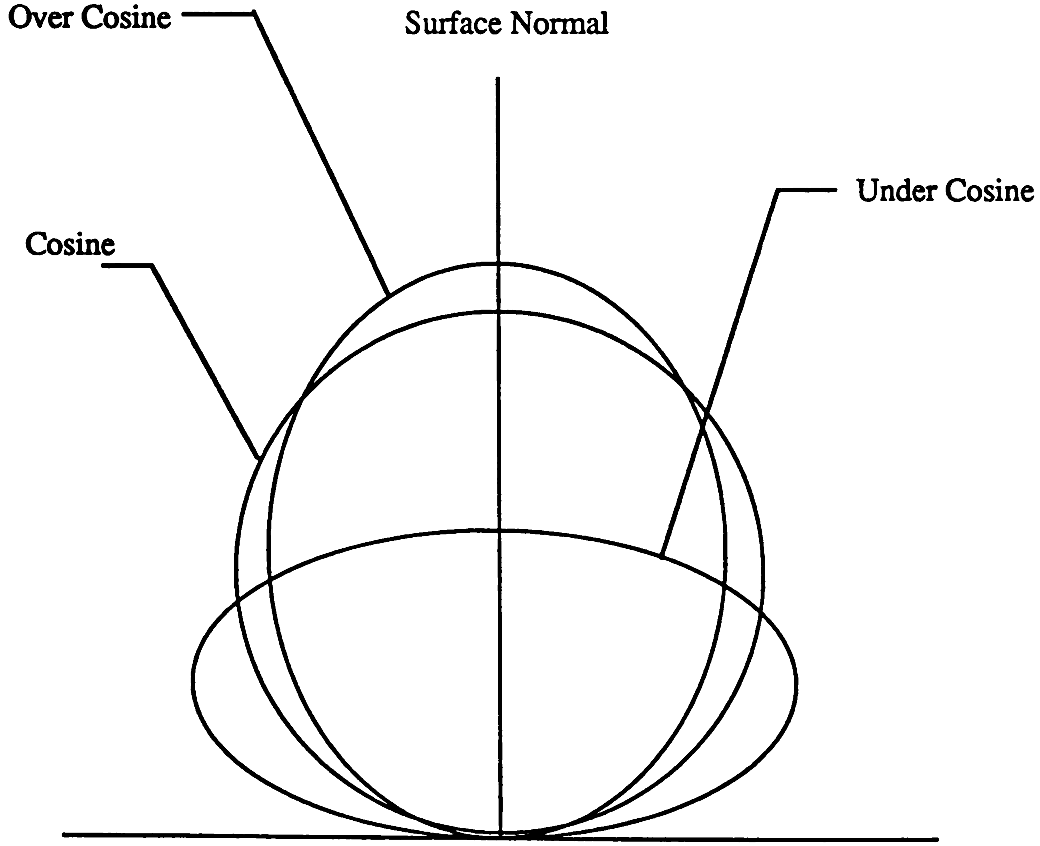

Figure 4-1 Angular Distribution of Sputtered Atoms from a Polycrystalline Target [57]

In a study by Olson [58], for normal ion incidence and different ion energies, Fe-Ni and Ni-Cu alloys were sputtered and the emitted atoms were collected at various angles. The results showed that at lower energy (< 100 eV), preferred ejection of the lighter mass atoms in the target normal direction occurred. The phenomenon was not unexpected since, when only a few atom collisions become involved, the fact that a lighter mass atom can be backscattered from a heavier one, but not vice versa, must reveal itself in the observed preferential ejection of lighter masses in the upstream ion beam direction.

However, at higher energies (200-1000 eV), the experimental results were contradictory. Sputtered Fe-Ni alloy led to a preferred normal ejection of heavier components, while for Ni-Cu alloy, there was no change in preferred normal ejection of the lighter component. Thus, for higher ion energies (> 200 eV), the results indicate that factors other than mass, such as binding energy and crystal structure, become dominant and determine the angular distribution of the component. This effect implies that in film deposition at low gas pressure, the composition depends upon the geometry and relative position of the target and substrate.

The geometric relationship of substrate and target surface in this study is shown in Figure 4-2, there are two collection positions on the substrate. One is at the position of the target center axis, and the other is at a radius of 2.5 cm, angle zero degrees in the polar coordinate system relative to the axis of the target. Note that the eroded target surface angle is measured from a target that has been sputtered for about 15 hours, as shown in Figure 4-3. Assume that the distribution of the sputtered atoms from the inclined target surface follows the cosine law with respect to the surface normal. Then, referring to Figure 4-2, it shows that the original preferred normal ejection constituent will be preferably collected at the center position of the substrate, and this effect will increase as the target erodes.

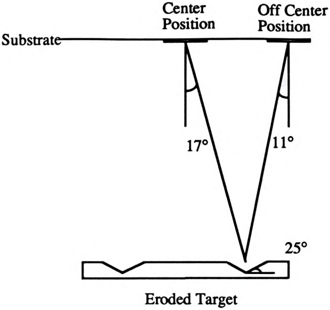

Figure 4-2 The Geometric Relationship of Samples and Target Surface

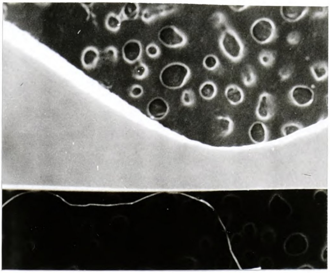

Figure 4-3 An Eroded Target with its Localized Erosion Angle

4.1.3 The Development of Target Surface Topography

A topography will develop upon heavily ion irradiated surface [59]. Sputtering creates at least atomic scale discontinuities (< 100 Å) at the surface, and such effects may be observed for individual ions and for fluences up to the order of 10^{16} ions/cm^2, depending on ion species and target materials. When ion fluence increases above the order of 10^{17} ions/cm^2, the density of atomic scale discontinuities increases, and the bombardment induced defect features become microscopically observable and range in sizes of 100-10,000 Å. Then, local variations in sputtering yield occur resulting in major changes in surface topography, as evidenced by the development of topographic features such as etch pits, cones and ripples. At a very large ion fluence, i.e., above the order of 10^{19}-10^{20} ions/cm^2, sputter etch effects may induce differential dimensional changes in the order of sub-millimetric size. At such levels of dimensional change, theoretical models of morphology change become meaningful.

In this study, the sputtering target had a bombardment area of about 4π cm^2 and the ion current ranged from 60 mA to 500 mA. Therefore, the ion current densities ranged from 5 to 40 mA/cm^2 and in other units from 3.15×10^{16} ions/cm^{2}sec to 2.5×10^{17} ions/cm^{2}sec. Since the deposition time was at least 20 minutes for every test run, the fluence was above the order of 10^{19} ions/cm^2 for every process condition. Thus, the macroscopic theory is applicable to this study. Figure 4-4 indicates the grains and grain boundaries of a target before ion bombardment. Figure 4-5 and Figure 4-6 show the topography of the target surface after about 15 hours ion bombardment. Ridges and cones can be easily found in the figures.

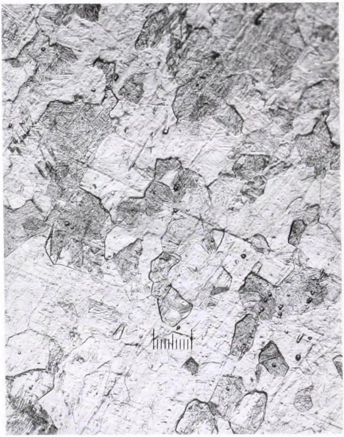

Figure 4-4 The Grain Structures of Target Surface before Ion Bombardment (100 ×)

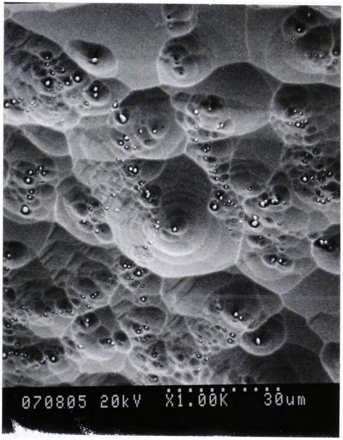

Figure 4-5 The Topography of a Target Surface Sputtered for 15 Hours

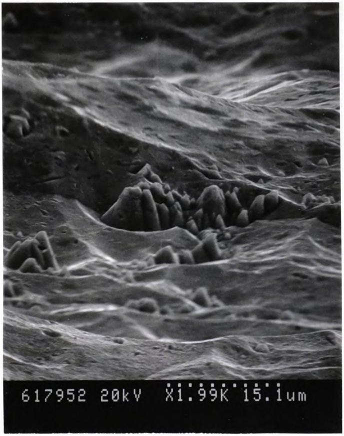

Figure 4-6 The Cone Structure on the Target Surface

A first-order erosion theory, ignoring secondary effects such as local flux variations, atomic redeposition and surface atomic transport, was proposed by Carter and Barber [60, 61], and successfully predicted the formation of topographic features, in particular cones, which have been experimentally observed on the macroscopic sputtering scale and at the microscopic level. The basic assumption of this theory is that sputtering yield varies with the incident angle and the angle of maximum sputtering yield is present within initial protuberances above the mean surface. For initial low roughness surface, the high angle surfaces required for this theory can form from either contaminant protection, as shown in Figure 4-7 [62], or from grain boundaries, etch pits and any other departure from flatness. If the initial surface is itself rather rough, then ridge and conical structures may develop from the beginning.

Also, the development of surface topography is sensitive to the bombarding ion current density. For example, the surface of a copper crystal can become covered with cones when the ion current density is > 100 $\mu A/cm^2$, but, with the same total fluence with a ion current density of < 100 $\mu A/cm^2$, only occasional cones are produced [59]. Furthermore, Kaufman and Rossnagel [63, 64] reported the average cone spacing is proportional to the inverse square root of the bombarding ion current density. It means that a higher ion current density causes a higher density of cones on the bombarding surface.

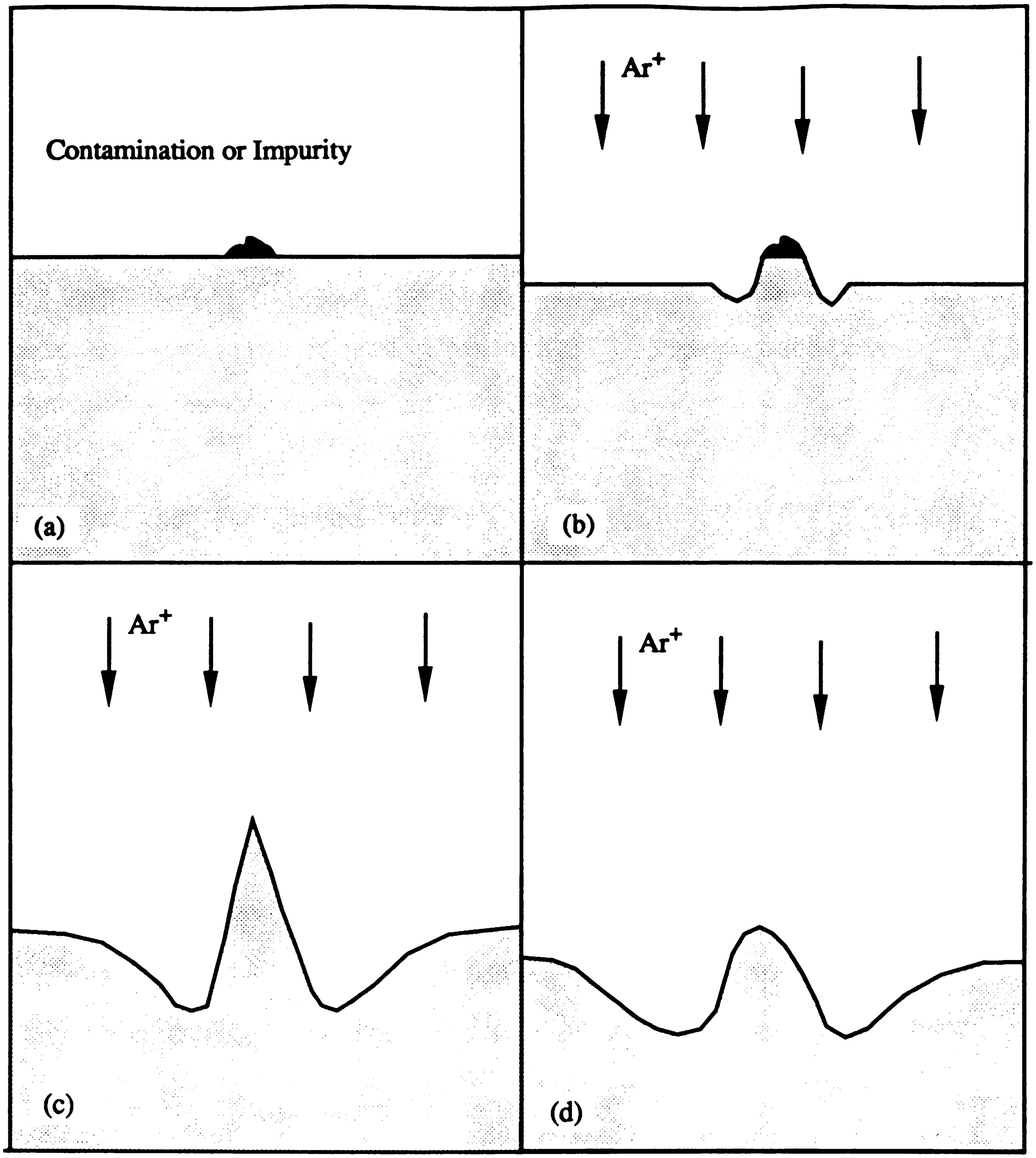

Figure 4-7 Schematic Diagram Showing Impurity-Induced Cone and Subsequent Pit Formation [62]

An important phenomenon related to surface topography is the variation in total sputtering yield. Because of the increase in yield caused by oblique incidence (Figure 2-12), the feature structured surfaces lead to enhanced emission; but recapture of ejected particles at these ridges or cones may compensate for this effect. Littmark and Hofer [65] considered this problem and found the total sputtering yield to be larger than that for flat surfaces. Only in the case of steep, needle-like cone structures (incidence angle > 70°) will the recapture of released particles prevail and the yield be smaller. However, there are no studies concerning the relationship between surface topography and the changes of component sputtering yield in the sputtering of alloy .

4.1.4 Resputtering of Growing Thin Films

Figure 2-15 shows that the substrate is inevitably subjected to impingement by many species during the deposition process, such as ions and neutral atoms, so there always exists a certain amount of resputtering of the growing film.

The source of neutral atoms is the primary bombarding ions reflected from the target surface. Vossen [66] reported that these bombarding ions have a high possibility of being neutralized prior to impacting the target. Then, they may be reflected as neutral atoms, not ions, without being influenced by the electric field over the target surface. The amount of reflection is an inverse function of primary bombarding energy because this effect competes with ion implantation. At low primary energies (< 1000 eV), reflection fractions as high as 0.4 have been observed, whereas at high primary bombarding energies (> 1000 eV) typical reflection fractions are of the order of 0.05 [66]. However, the reflected atoms have a wide energy spectrum which make it difficult to estimate the incident flux of these particles.

In magnetron sputtering, the magnetic field does not directly affect the ion motion. Nevertheless, because of electrostatic attraction, the ions move with the electrons keeping the plasma neutral. Theoretically, in a conventional magnetron, most of the discharge is confined close to the cathode surface and, therefore, bombardment of growing film by electrons and ions is minimized. In practice, substrate bombardment could be significantly increased by "unbalancing" the magnetics [67]. In an unbalanced magnetron, the flux from the north pole is unequal to that entering the south pole, as indicated in Figure 4-8 [68]. The flux from the central is less than that of the outer magnet. Therefore, the system gives large ion currents and large electron currents to the substrate. Electrons are channeled along field lines extending from the discharge region to the substrate. The unbalanced magnetron is capable of giving ion fluxes at the substrate that are larger than the flux of sputter atoms. The resputtering ion flux is very dependent on the magnetic field configuration, discharge current; however, it is roughly independent of the target composition, gas pressure, and gas composition [67, 68].

Because magnetic field lines are difficult to focus, it is very difficult to construct a perfect, "balanced" magnetron. Thus, magnetron sources are always accompanied by substrate bombardment by ions and electrons from the plasma discharge.

According to the IBAD results by Chang [26], the sputtering yield of Ti in the deposited amorphous TiNi thin film is higher than that of Ni ($Y_{Ti} > Y_{Ni}$). Therefore, Ti will be preferentially removed from the film. Furthermore, unlike the target, the surface of the growing film is constantly being replenished with new materials of the cathode composition, so an "altered layer" cannot form and the "steady-state" cannot never be established. Thus, the depletion amount of Ti will increase as the resputtering effect increases.

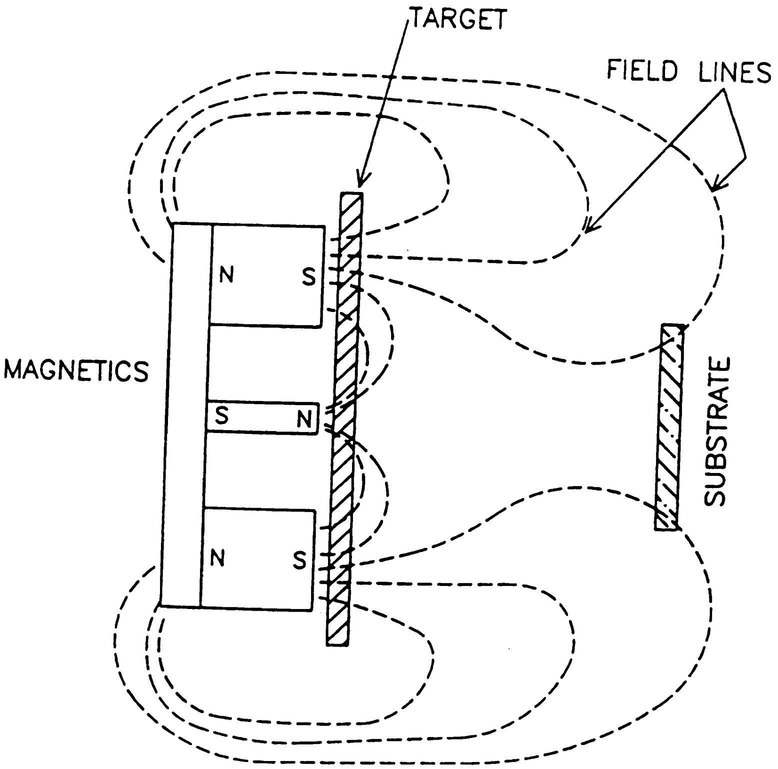

Figure 4-8 Schematic Representation of an Unbalanced Magnetron [68]

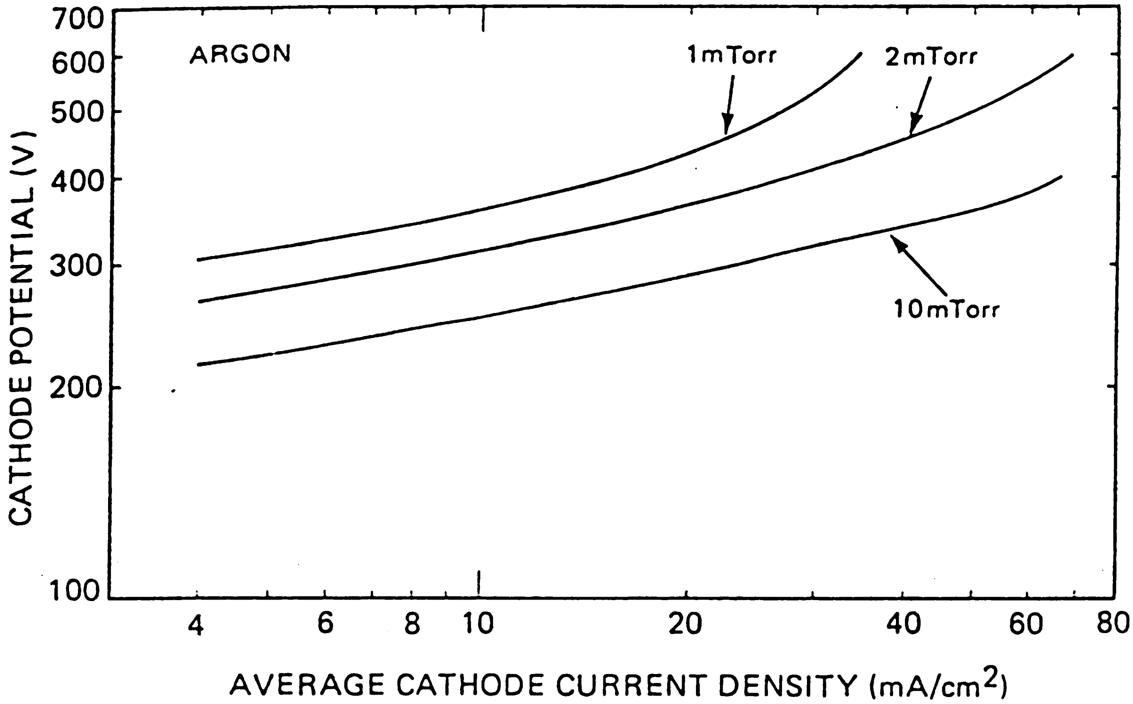

Figure 4-9 A Typical Voltage-Current Characteristic for Planar Magnetron Cathode at Various Pressures [69]

4.1.5 Planar Magnetron Source

The typical voltage-current characteristics for a planar magnetron source is shown in Figure 4-9 for various pressures. These curves have been empirically found to follow the relation [69]

$$I = kV^{n} \qquad (4.6)$$

where I is the cathode current (or current density) and V is the cathode voltage, k is a constant, and the exponent n is a constant ranging from 3 to 15. The constants of k and the exponent n are dependent on the type of magnetron used, the target materials, the gas species, and the gas pressure. Usually, the more efficient the electron trapping in the plasma, the higher the exponent n.. Also, since the power (W) is the product of cathode voltage and current, Equation (4.6) becomes

$$W = IV = kV^{n+1} \qquad (4.7)$$

where k and n are the same constants as in Equation (4.6).

Thus, for a given target material and cathode configuration, a family of current-voltage curves versus pressure can be obtained. This enables a suitable operating point to be chosen for a given voltage or power value.

However, as the target erodes, the plasma impedance changes because of the increased strength of the parallel component of the magnetic field at the surface of the target [70]. This indicates that the exponent n in Equation (4.6) will increase as the process continues. For most applications, this does not pose a problem. But, in the present experiment, the magnetron source used for sputtering is relatively small (5 cm in diameter), and the change of the exponent n causes an evident change of the process condition during the deposition. This may induce other factors that have to be considered for the control of composition of the deposited thin film.

As mentioned in section 3.2.3, in this study the deposition process can be controlled at power, voltage, or current regulation mode, meaning that power, voltage, or current is kept at a constant throughout the deposition periods. In magnetron sputtering, from Equation (4.7), the *k* and exponent *n* both are constants at a specific process pressure, and controlling the process by power or voltage has the same effects. But, actually, the exponent *n* will increase during deposition even though under the same pressure. Thus, when the process is controlled by power regulation mode, the voltage will decrease with increasing exponent *n* to maintain a constant power; when the process is controlled by voltage regulation mode, the discharge current increases as the exponent *n* increases.

4.2 Effects of Process Parameters on Thin Film Composition

There are four process parameters being surveyed in the present experiment, they being plasma voltage, plasma power, process pressure, and working distance between target and substrate, respectively. Before these tests for the process parameters, a test was conducted to determine the significance of target erosion effect on the thin film composition. The final composition of the deposited film for every process condition is determined by the combined effects of various factors considered in the first part of this chapter. In addition to the complexity of the glow discharge sputtering environment and the formation of target surface topography features by high bombarding fluences, the continuous changes of strength of the magnetic field (i.e., the exponent *n* in Equation (4.6)) make the process conditions non-steady-state and extremely complicated. Most of the experimental results can be only interpreted qualitatively at this stage. However, valuable information concerning the fabrication of TiNi thin films using a magnetron source TORUS®-2C can be obtained.

The sputtering target has a finite life and will eventually erode through. Also, the development of topographies on the target surface with processing will affect the deposited film composition. Usually, the amount of target erosion is estimated by the value of (time × current). Since the deposition processes are normally operated under 1000 eV in magnetron sputtering, the amount of erosion can also be estimated by (time ×

power) due to the linear increase of sputtering yield with voltage in this energy range. A table of target histories for the test factors affecting deposited film composition is shown in Table 4-2. The values recorded in this table are the products of time and power. There was a total of two targets being used in this study. Approximately, the total target life is about 3800 W·hour, and it can be used up to 2800 W·hour without eroding through in the deposition of TiNi thin film by magnetron source TORUS®-2C.

Table 4-2 Histories of Targets in the Different Factor Tests (W·hour)

Test	Target Number	Used Before This Test	Used in This Test	* How Much Left
Target Erosion	1	1000	1050	1750
Plasma Voltage	1	2050	550	1200
Plasma Power	2	0	500	3300
Gas Pressure	2	500	900	2400
Working Distance	2	1400	450	1950

* Total target life is about 3800 W·hour and about 2800 W·hour available .

4.2.1 Effect of Target Erosion

One disadvantage of using a planar magnetron source is the localized erosion of the target. This series of experiments is thus designed to study if non-uniform erosion effects can have influences on film composition. The experimental procedure for this test was controlled by power regulation mode while keeping the other process parameters such as pressure and distance constant. Then, thin film samples were continuously collected at different process time periods. The process conditions and their compositional results are shown in Table 4-3. Since the processes were controlled by power regulation mode, the decreasing of voltage and increasing of discharge current during processing were expected, as predicted by Equation (4.7). However, the quick decrease of voltage during every deposition was unexpected.

A graph of the target erosion effect on the composition of thin films is shown in Figure 4-10. In this graph, thin film with the highest Ni concentration was found at the beginning of the process, then went to a stable region, and at the fourth hour, a Ti-rich thin film with respect to the target alloy composition was produced.

Assuming that all the process parameters were constant during deposition, the changes of composition with target erosion time could be attributed to one cause — changes in target surface topography, macroscopically and microscopically. Due to the preferential ejection of the high sputtering yield component at the beginning of the process, the sputtered flux leaving the target surface has a higher concentration of the high sputtering yield component. The high sputtering component in TiNi alloy is Ni, as discussed in section 4.1.1. So the first thin film sample had the highest Ni concentration. After the target "wear-in" for approximately 20-30 minutes, a steady-state is reached and the sputtered flux has the same composition as the target alloy. But, since the resputtering effect cannot be avoided and causes the depletion of Ti, the deposited thin films still possessed a higher Ni concentration than the target alloy. Finally, the target surface was built up to an extent which could change the stable region.

Deposition time for each sample = 60 min
Power = 250 Watts
At Center Position
Distance = 5.08 cm
Pressure = 0.41 Pa

Working Voltage	790V→ 739 V	738 → 689 V	687 → 643 V	642 → 607 V
Cathode Current	314 → 336 mA	340 → 365 mA	367 → 387 mA	388 → 400 mA
Time Interval	1st hour	2nd hour	3rd hour	4th hour
Thickness	91683 Å	87973 Å	86088 Å	82514 Å
Dep. Rate	1530 Å/min	1465 Å/min	1435 Å/min	1375 Å/min
Composition (Ni at%)	51.73±0.14%	50.94±0.22%	51.10±0.20%	50.25±0.12%

Target Composition (Ni-Ti at%) 50.59 - 49.41 at% ± 0.04 Ni

Table 4-3 Process Condition for Target Erosion Test and the Compositional Results

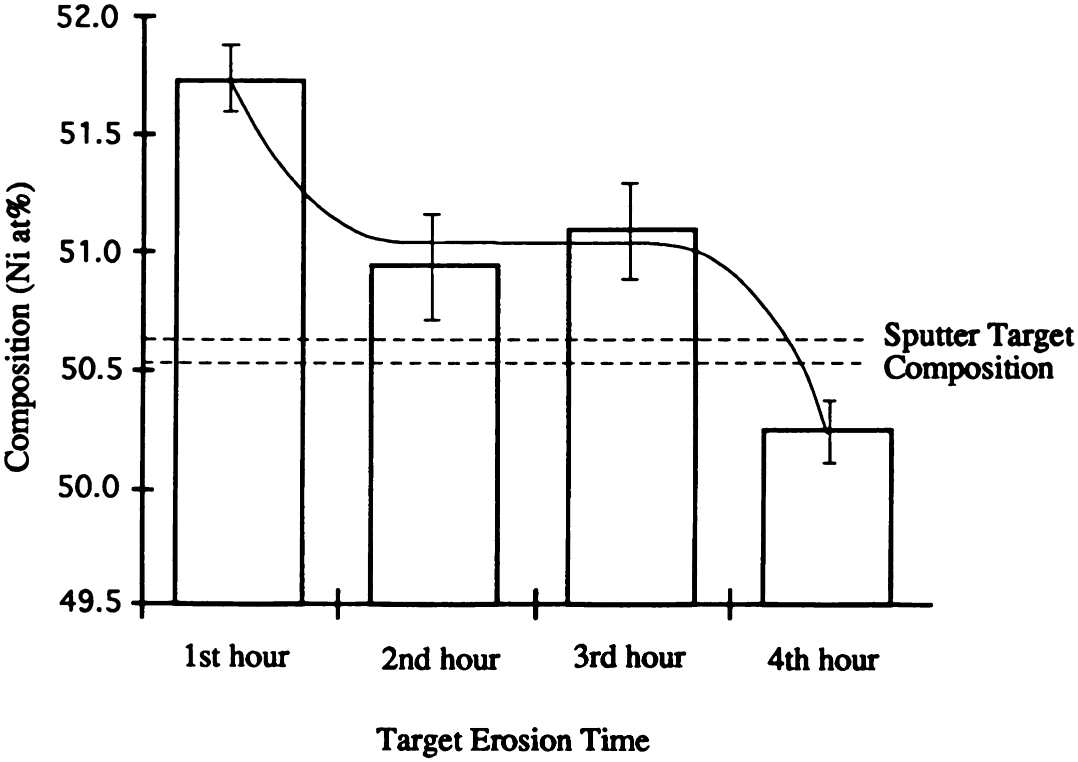

Figure 4-10 Composition Change as a Function of the Target Consumption

There are two effects resulting from the development of surface topography. Macroscopically, the change of target surface angle will cause a different angular distribution of sputtered atoms. As mentioned in section 4.1.2 and referred to Figure 4-2, this effect may cause the original preferred normal ejection constituent to be preferably collected. Microscopically, the formation of target surface topography features such as ridges, cones, and etch pits could change the total sputtering yield and the component sputtering yield. Because of the absence of experimental data concerning the effect of surface topography on the component sputtering yield, it is difficult to determine which component is preferentially ejected. Nevertheless, the experimental results in this study show that the combination of macroscopically and microscopically topographic effects produced a Ti-rich thin film.

However, the above discussion is not totally applicable because the process parameters, such as voltage and discharge current, were not kept at a constant during deposition. Thus, in addition to the surface topographic effect, there is another factor that must be taken into consideration, i.e. if the depositions were always processed under a steady-state, the sputtered flux leaving the target surface always carried the same composition as the target alloy.

At the beginning of the process, the sputtered flux had a higher Ni concentration as did the first sample. After about 20-30 minutes, steady-state was established at a specific voltage and an altered layer formed with a Ti-enrichment composition related to the component sputtering yield ratio Y_{Ni}/Y_{Ti} at this specific voltage. In a short time (1~2 minutes), the voltage dropped and the original altered layer had to change to a new altered layer having another Ti-rich composition related to Y_{Ni}/Y_{Ti} at the second voltage to establish the steady-state. Since the value of Y_{Ni}/ Y_{Ti} decreases with decreasing energy, as discussed in section 4.1.1, the altered layer will become less Ti-rich with decreasing energy. Thus, the sputtered flux will carry a higher Ti concentration during the transition period than when it did at steady-state.

Previous experimental results for other alloys showed that the removal of one to two altered layer thicknesses was necessary to reach the steady-state condition [41]. Usually, the thickness of an altered layer is determined by the maximum penetration depth of the primary ions, and a combination of preferential sputtering at the surface and a transport mechanism. The transport mechanism describing the propagation of the changed surface composition deeper into the material includes thermal diffusion and/or radiation enhanced diffusion, and erosion of the target due to sputtering [71]. Radiation enhanced diffusion means that under ion bombardment, many lattice atoms are displaced in the course of the collision cascade creating vacancies, interstitials and finally larger defects, all of which enhance diffusion. Ho [71] extended a kinetic analysis of preferred sputtering [72] by including radiation enhanced diffusion. Solutions for the steady-state showed that the composition of the altered layer varied with the distance from the surface in a simple exponential manner, and the effective altered layer thickness δ in the alloy was $\delta = D/u$, where D is the diffusion coefficient, u is the velocity of the receding surface (erosion rate). The expression of δ was already predicted by Pickering [73]. Also, Ho [71] estimates the magnitude of diffusivity from measurements [72] yield values of the order of 10^{-16} cm^2/sec for Cu-Ni alloy. However, since the dc plasma sputtering system usually has a high sputtering rate (>10 Å/s), the thickness of altered layer determined by diffusion effect is not evident.

Ion bombardment of an alloy generally produces an altered layer whose composition at thermal equilibrium no longer corresponds to a single-phase alloy. Thus, precipitation of a component cannot be excluded, especially for the TiNi alloys. The existence of precipitates will cause selective sputtering, based on different erosion rates of different phases. For high fluences ($\geq 10^{19}$ ions/cm^2), the interplay of selective sputtering and the formation of surface topography features finally leads to a steady-state condition. For selective sputtering being the dominant process, steady-state conditions will be reached after sputter erosion of a layer on the order of a few grain diameters, as has been demonstrated for the case of MgO/Au cermets [74]. If topography effects dominate, an equilibrium is reached after development of a quasi steady-state surface topography, i.e., when the rates of cone formation and annihilation are equal. In a study for sputtering Ag-Co and Ag-Ni, the steady-state conditions were reached after the removal of a layer much smaller than the average grain diameter [75], indicating the dominance of topography effects over the selective sputtering. However, no matter which effects dominate, sputtering of such a solid is marked by a long transition time before steady-state conditions are reached.

Thus, in this study, when processes were controlled by power regulation mode, the sputtered flux had high possibility of carrying more Ti than at steady-state due to the long time transition periods, and the total amount of Ti was decided by the difference of the component sputtering ratio between energies from the process beginning to the end. If a function of component sputtering yield ratio Y_{Ni}/Y_{Ti} versus energy is obtained, the slope of this function during the energy interval determines how significant this effect is. Therefore, except for the first sample, the composition of the other three thin film samples can be explained in this way. Remember that the resputtering effect would cause the depletion of Ti in the deposited thin films even though the sputtered flux is Ti-rich.

Therefore, there are three competing factors affecting the final film composition, the macroscopic and microscopic changes of target surface topograpy, and the non-steady-state effect. However, at this point, it is difficult to distinguish which one is the dominant factor in this test.

4.2.2 Effect of Plasma Voltage

For glow discharge sputtering process the plasma voltage (cathode potential) is the most important process parameter. It determines the energies of the bombarding ions and is related to the sputtering yields of the sputtered materials. In this test, the process conditions were controlled by voltage regulation mode and at three different voltage values: 500V, 625V, and 750V. Both the gas pressure and working distance were kept constant at 0.53 Pa and 50.8 mm, respectively. Detailed process conditions and their compositional results are shown in Table 4-4. Notice that the deposition time for every process condition was different and adjusted to deposit thin films of at least 3 μm in thickness allowing for accurate composition measurement in EDS analysis. Also, a graph of composition as a function of plasma voltage is shown in Figure 4-11. It shows that the deposited thin films had higher Ni concentration than the target alloy and the Ni concentration increased with increasing energy.

Unlike the target erosion test, the thin film samples in this test and the next three tests were all deposited after a steady-state was attained, following the experimental procedure described in section 3.3. In the present experiment, since the processes were controlled by voltage regulation mode, the changes of exponent n can alter the discharge current during deposition (Equation (4.6)). The changes of discharge current may influence the target surface topography and change the sputtering yields. However, the change rate of discharge current is slow and a steady-state condition can be easily recovered during every change. Thus, it is reasonable to assume that a steady-state condition was maintained for every process condition during deposition, i.e., the sputtered flux leaving the target surface always carried the same composition as the target alloy.

500 V	0.53 Pa, 35→38 W, 63→70 mA, time=150 min, D=51 mm
Position Thickness Dep. Rate Composition (Ni at%)	Center 31394 Å 209 Å/min 52.79±0.11%
625 V	0.53 Pa, 98→119 W, 151→184 mA, time=120 min, D=51 mm
Position Thickness Dep. Rate Composition (Ni at%)	Center 77974 Å 650 Å/min 56.02±0.11%
750 V	0.53 Pa, 128→162 W, 165→211 mA, time=90 min, D=51 mm
Position Thickness Dep. Rate Composition (Ni at%)	Center 74146 Å 824 Å/min 56.12±0.07
Target Composition (Ni-Ti at%) 50.59 - 49.41 at% ±0.04 Ni	

Table 4-4 Porcess Conditions and the Compositional Results in the Voltage Effect Test

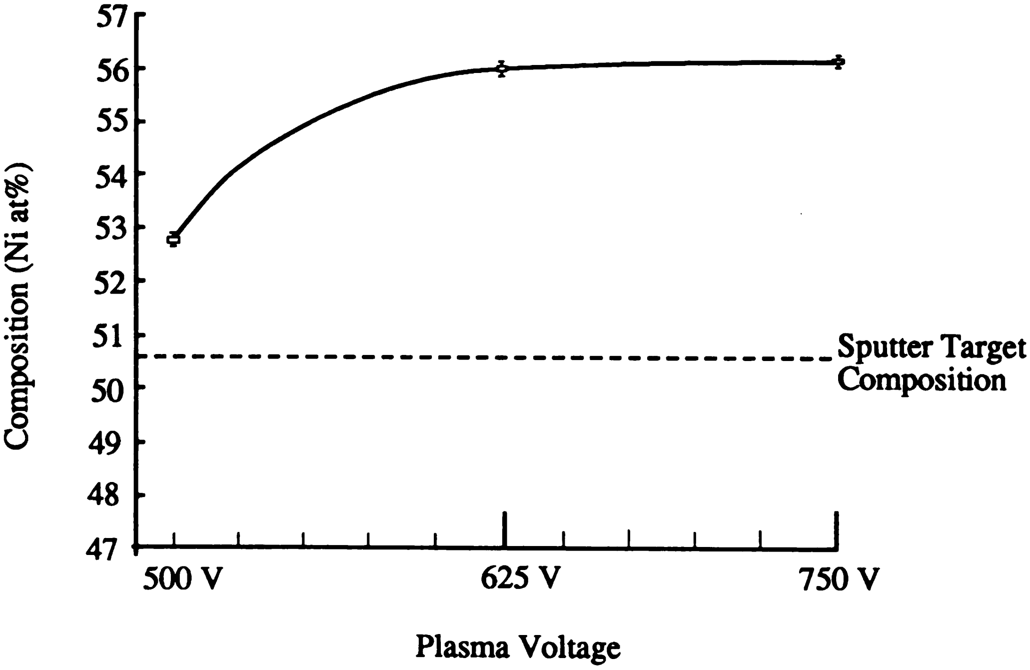

Figure 4-11 Composition Change as a Function of Plasma Voltage

Since the deposition processes were under steady-state condition and the gas pressure was kept constant, two other factors are left to be considered as sources for causing the composition change: the effects of angular distribution of sputtered atoms, and resputtering. An important issue which must be noted here is that thin films deposited in this test were made after the target erosion test and the same eroded target was used for these depositions. In section 4.2.1, the macroscopic target surface change led to a different angular distribution of sputtered atoms and could be a potential factor causing Ti-enrichment in thin films. If this were true, thin films deposited in this test must be Ti-rich. However, the opposite results were found in this test using the eroded target. This implies that when compared to other factors, such as resputtering effect and changed sputtered flux effect, the change of angular distribution of sputtered atoms due to the target localized erosion effect is not very significant.

As discussed in section 4.1.4, the neutral atoms causing resputtering come from the primary bombarding ions reflected from the target surface. Thus, the larger number of bombarding ions induces more neutral atoms and increases the resputtering effect. Also, the depleted amount of Ti increases as the resputtering effect increases. Since the number of bombarding ions can be estimated by the product of the discharge current and the deposition time, the resputtering effect resulting from the neutral atoms can be then decided. Referring to Table 4-4, the number of bombarding ions at 625 V was about twice as many than those at 500 V. Therefore, more Ti was resputtered from the thin film deposited at the 625 V process condition. Under conditions of 625 V and 750 V, the numbers of bombarding ions were similar. Thus, the resputtering effect was almost the same, as were the compositional results. The energies of the neutral atoms should influence the resputtering rate. However, Chang's study [26] showed the component resputtering yield ratio Y_{Ti}/ Y_{Ni} had little change when it was above 500 eV. So basically, the ratio can be assumed to be constant at these energy levels.

From this test, it was found that the change of angular distribution of sputtered atoms was not evident when compared to the other factors. Also, the resputtering effect can induce a significant composition difference in the deposited thin films.

4.2.3 Effect of Plasma Power

Theoretically, plasma power is not thought to be a factor affecting the compositional shift between thin films and target alloy in magnetron sputtering deposition. However, the magnetron sputter-deposition processes controlled by power regulation mode have been practically used in the semiconductor manufacturing industry because of the safety and sputtering rate issues. So, it is worthwhile to verify if processes controlled by power regulation mode can be found to cause any shift in thin film composition. If no shift is evident, the power regulation mode may be used to control the deposition processes in a practical manner.

Table 4-5 shows the process conditions and the compositional results in the plasma power effect test. Processes were controlled by power regulation mode and processed at 150 W, 300 W, and 450 W, respectively. Pressure, 0.44 Pa, and working distance, 50.8 mm, were always kept constant at the three power levels.

There is a set of data for each of two different positions on the substrate. One is at the position of target center axis, the other one is at radius 25.4 mm, angle zero degree in the polar coordinate system relative to the center position. The thickness profile over the substrate showed a maximum at the center. Maissel [76] suggested that the conditions for ensuring better uniformity of deposition are obtained when a plane cathode is about twice as large as hat of the substrate used. Because in the study, thin films were deposited by a 50.8 mm sputtering cathode, it is expected that a uniform film thickness and composition cannot be attained over the substrate of the same size as the cathode source.

150 Watts	0.44 Pa, 947→830 V, 153→175 mA, time=80 min,D= 51 mm	
Position	At Center	25mm off axis
Thickness	88,959 Å	60,984 Å
Dep. Rate	1112 Å/min	762 Å/min
Composition (Ni at%)	52.32±0.05%	51.59±0.26%
300 Watts	0.44 Pa, 1008→918 V, 294→324 mA, time=40 min, D=51mm	
Position	At Center	25mm off axis
Thickness	78,293 Å	56,358 Å
Dep. Rate	1957 Å/min	1408 Å/min
Composition (Ni at%)	49.72±0.30%	50.64±0.19%
450 Watts	0.44 Pa, 932→983 V, 482→465 mA, time=20 min, D=51 mm	
Position	At Center	25mm off axis
Thickness	58,756 Å	56,433 Å
Dep. Rate	2938 Å/min	2821 Å/min
Composition (Ni at%)	51.15±0.12%	51.55±0.16%
Target Composition (Ni-Ti at%) 50.59 - 49.41 at% ± 0.04 Ni		

Table 4-5 Process Conditions and the Compositional Results in the Power Effect Test

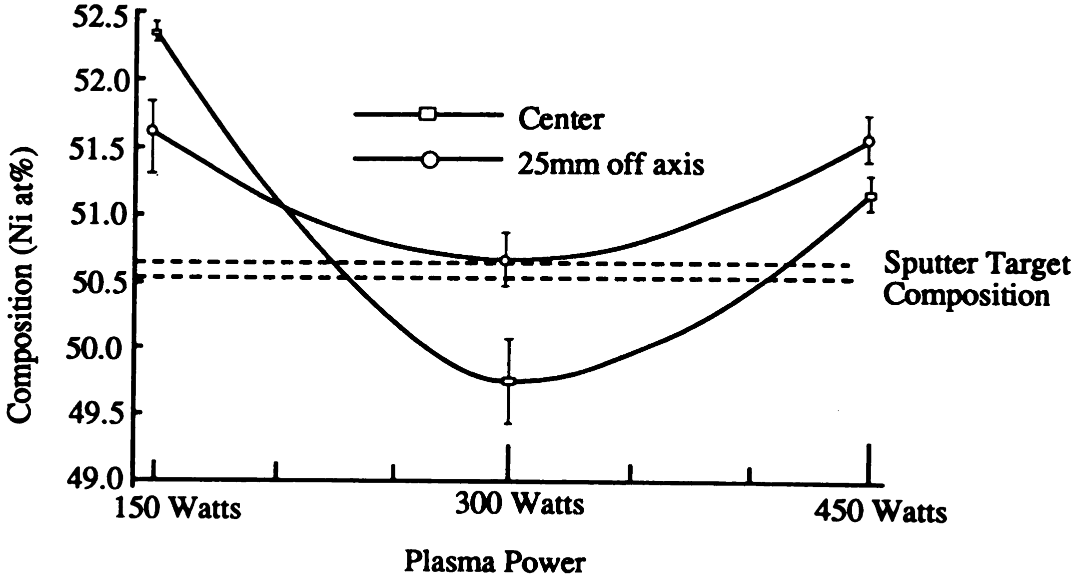

Figure 4-13 Composition Change as a Function of Plasma Power

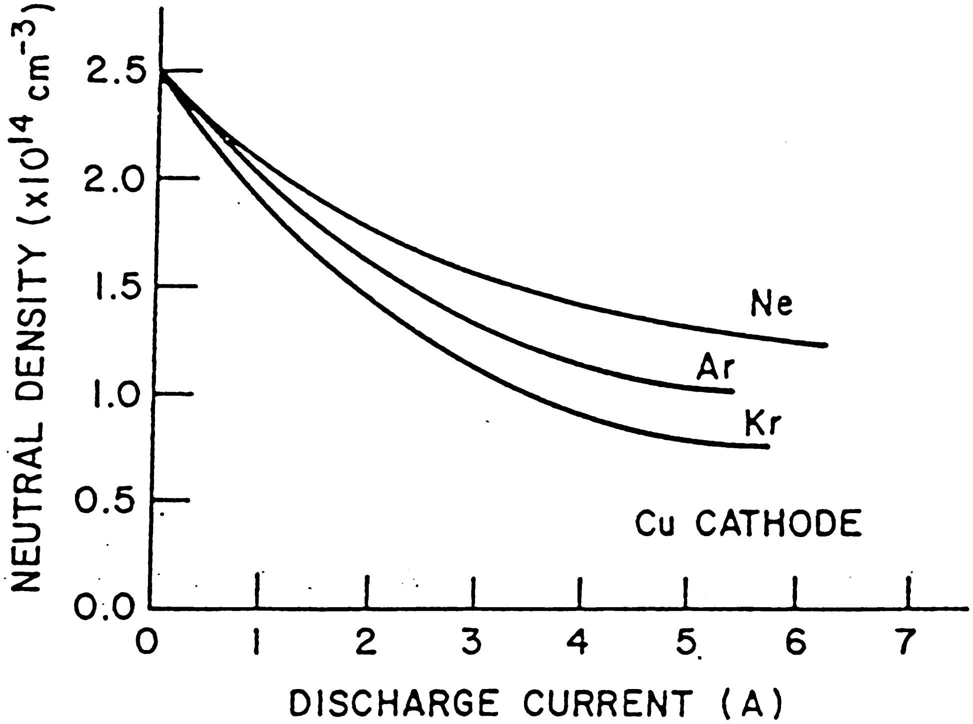

Figure 4-12 Local Gas Density Measured Near the Magnetron Cathode During the Sputtering of Cu in Ne, Ar, and Kr as a Function of Discharge Current [78]

Note that at 450 W, the voltage increased during deposition. This result was opposite from that obtained at conditions of 150 W and 300 W in this test and at 250 W in the target erosion test, whose voltage increased during deposition. One possible reason causing this abnormal phenomenon at 450 W is the rarefaction effect. One characteristic of magnetron plasmas is a high level of sputtering of the cathode. Sputtered atoms emitted from the bombarded surface can have gas-phase collisions with background gas atoms and, as such, transfer some of their energy to the atoms through elastic collisions. The effect is known as thermalization. During this process, significant amounts of thermal energy are transferred to the gas atoms, and their temperature can rise significantly [77, 78]. Because of the higher atom velocities near the cathode, the gas may become rarefied field, and the local density near the cathode can decrease. This is shown in Figure 4-12 [78]. This effect is strongly dependent on the thermal conductivity of the gas, the sputter yield of the target materials, and the applied discharge power. Ions in the plasma are created by ionization of the background gas. Driving down the local gas density by sputtered atom heating results in a more resistive plasma. Thus, the local gas density near the cathode decreases with increasing discharge current. This implies the creation of a more resistive plasma, i.e., the decrease of exponent n in Equation (4.6). This may cause the voltage increase during deposition when the process is controlled by a high power, as at 450 W in this test.

A graph of composition as a function of plasma power is shown in Figure 4-13. It shows that at 300 W and the center position, a Ti-rich (with respect to the target alloy) thin film could be produced; while at 150 W and 450 W, Ni was always the major component in the deposited films.

As discussed in section 4.1.4, resputtering effect results from the bombarding of neutral atoms, which are the primary bombarding ions reflected from the target surface. Since the center position has a greater chance of being bombarded by the reflected neutral atoms than the off center position, thin films deposited at the former position will have higher Ni concentrations than those deposited at the latter position. However, in addition to the neutral atoms, the other resputtering source is the ion flux introduced by the "unbalanced" magnetron. Referring to Figure 4-8, the ion flux from the central is less than that of the outer region. Thus, the outer region will suffer more ion flux bombardment and cause a greater amount of Ti depletion from the deposited films than the center position, and this is opposite to that caused by neutral atoms. The resputtering ion flux is very dependent on discharge current. Thus, the discharge current will determine which resputtering source dominates during the deposition process. The experimental results from this test and the next test (section 4.2.4) showed that when the discharge current was above about 250 mA, the outer region of the substrate would sustain more bombardment of ion flux and cause more loss of Ti component in the thin films.

Since the processes in the present test were controlled by power regulation mode, the arguments about the non-steady-state sputtered flux discussed in section 4.2.1 could be applied to the present test, i.e., if the voltage continuously decreased during deposition, the sputtered flux leaving the target surface had more Ti component than the target alloy, and vice versa. At 450W, the voltage abnormally increased during the deposition due to the rarefaction effect and resulted in the sputtered flux having more Ni component than the target alloy. Upon combining the resputtering effects, the deposited film composition possessed higher Ni concentration than the target alloy.

Referring to Table 4-5 and comparing the process conditions at 150W and 300W at the center position, both of them had very similar process conditions: the amount of decreasing voltage during deposition, the average plasma voltage, and the number of bombarding ions. Through the discussions of the above two tests, the compositions of the deposited films from these two process conditions were predicted to be very close. However, the experimental composition resulting from each condition was significantly different. Note that the only large difference between the two process conditions was the discharge current. As discussed in target erosion test, the sputtered flux carrying more Ti component than the target alloy is due to the existence of transition stages before the re-establishment of steady-state. And the total amount of the excess Ti is determined by the mechanisms occurring during the transition stages. For a multiphase material under high fluence sputtering, the topography effect is the dominant factor during the transition periods, i.e., steady-state is reached when the rates of cone formation and annihilation are equal. Unfortunately, the processes governing the evolution of surface topographies are still under discussion and inconclusive. The theoretical sputtering models for such systems are also not available. Thus, it is difficult to explain the detailed processes happening during the transition periods and its effect on the sputtering yields.

However, based on the process conditions of 150 W and 300 W in this test, one possible reason for the compositional differences between them is that at 300 W, the higher level of discharge current (~ 312 mA) resulted in higher density of cones on the target surface than those at 150 W (~ 166 mA), as described in section 4.1.3. Because the transition periods were determined by topography effect, it would take a longer time for the 300 W setting to establish the steady-state condition than it would the 150 W setting. Therefore, the sputtered flux at 300 W had more possibilities for a Ti-rich situation than that at the 150 W setting. The film deposited at 300 W thus had a higher Ti concentration than that deposited at 150 W. But, this is only a qualitative description of the comparison between the two process conditions. For a quantitative understanding of this effect, further experiments under defined conditions (Ultra High Vacuum, mass analyzed ion beam) are needed to obtain more information and insight into the development of the surface features, and the relationship with the sputtering yields.

4.2.4 Effect of Gas Pressure

After ejection from the target surface, the sputtered atoms are transported to the substrate in the deposition chamber. It is likely that the sputtered atoms can have collisions with background gas atoms. Also, the reflected neutral atoms responsible for the resputtering of growing films can suffer collisions with the gas atoms before reaching the substrate. Thus, the gas pressure plays an important role during transport for the sputter-deposition method. In this test, processes were controlled by voltage regulation mode. Thin films were deposited at 0.44 Pa, 0.64 Pa, and 1.01 Pa, respectively, while keeping the voltage at 600 V. Table 4-6 shows the process conditions and the compositional results in the pressure effect test. A graph of composition as a function of gas pressure is also shown in Figure 4-14. Since the processes were controlled by voltage regulation mode, it could be assumed the steady-state condition was maintained during deposition. Note that the phenomenon of non-uniform thickness and composition of thin films at different substrate positions can be explained by the arguments discussed in the above test.

However, unlike the plasma power effect test, the trend of changes of composition with pressure was different at the different substrate positions: at the off center position, Ni concentration in thin films linearly increased with gas pressure; while at the center position, a minimum Ni concentration could be found at the middle range of gas pressure (0.64 Pa). From the above test, the major cause resulting in the depletion of Ti at the off center position was the resputtering effect caused by the ion flux, which was introduced by the "unbalanced" magnetron. Since the resputtering ion flux is highly dependent on discharge current and roughly independent of gas pressure (section 4.1.4), the amount of depleted Ti increased with increasing discharge current. Because the discharge current increased with increasing pressure, the Ni concentration increased with increasing pressure at the off center position.

0.44 Pa	600V, 68→88 Watts, 106→141 mA, time=135 min, D=51 mm	
Position	At Center	25mm off axis
Thickness	69,335 Å	55239Å
Dep. Rate	513 Å/min	409 Å/min
Composition (Ni at%)	51.76±0.05%	51.05±0.23%
0.64 Pa	600 V, 159→195 Watts, 260→320 mA,time=80 min,D=51 mm	
Position	At Center	25mm off axis
Thickness	86,411 Å	69,748 Å
Dep. Rate	1080 Å/min	872 Å/min
Composition (Ni at%)	50.66±0.17%	51.68±0.28%
1.01 Pa	600 V, 235→290 Watts, 400→475 mA,time=80 min,D=51 mm	
Position	At Center	25mm off axis
Thickness	129,700 Å	91,859 Å
Dep. Rate	1621 Å/min	1148 Å/min
Composition (Ni at%)	52.41±0.18%	52.59±0.25%
Target Composition (Ni-Ti at%) 50.59 - 49.41 at% ±0.04 Ni		

Table 4-6 Process Conditions and the Compositional Results in the Pressure Effect Test

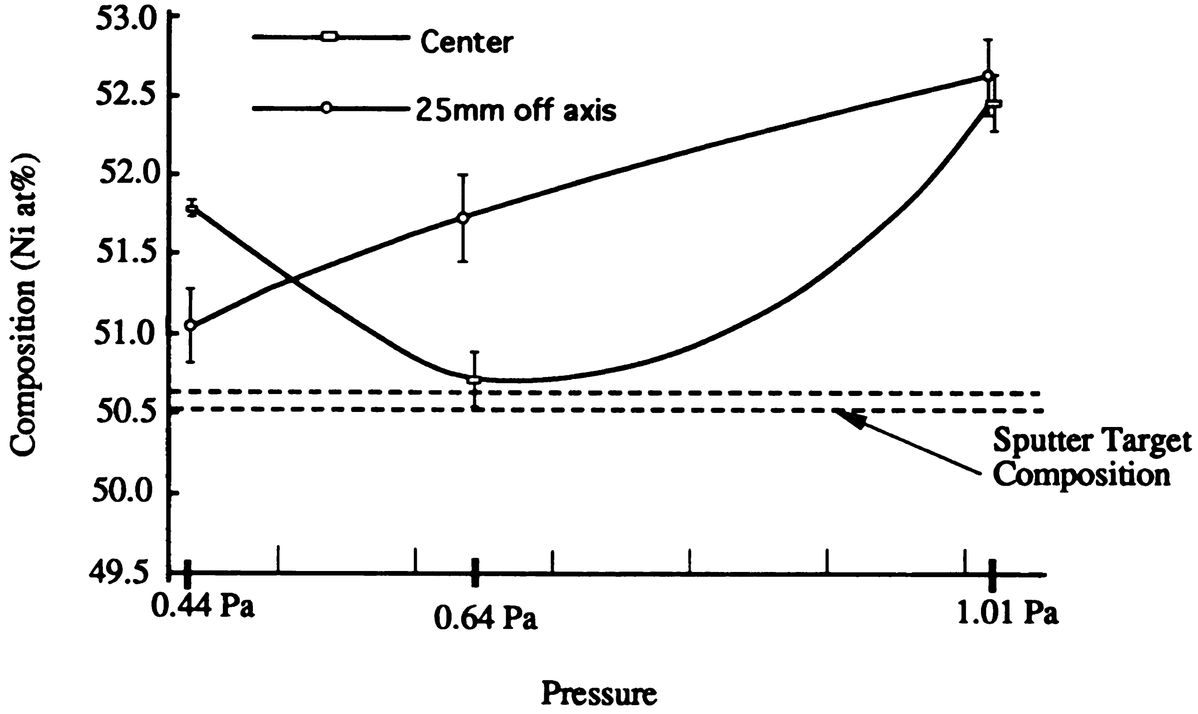

Figure 4-14 Composition Change as a Function of the Gas Pressure

At the center position, thin film compositions are determined by the deposition of sputtered atoms and the resputtering of neutral atoms. The gas pressure in the deposition chamber decides their collision numbers before reaching the substrate. More precisely, the parameter determining the number of collisions is the mean free path. From the mean free path equation:

$$\lambda = \frac{1}{\sqrt{2}\pi d_1 d_2 n} \qquad (4.8)$$

where n is the gas concentration, d_1 and d_2 are the molecular diameters of colliding atoms, one of them being the background gas atom's.

In this study, the sputter gas was Ar, with an atomic diameter of 3.67×10^{-8} cm, and the sputtered atoms were Ti and Ni, with diameters of 1.46×10^{-8} cm and 1.25×10^{-8} cm, respectively. Thus, the mean free path for Ar, Ti, and Ni at different pressures are shown in Table 4-7.

Table 4-7 The Mean Free Path of Ar, Ti, and Ni at Pressure of 0.44 Pa, 0.64 Pa, and 1.01 Pa.

	0.44 Pa	0.64 Pa	1.01 Pa
λ_{Ar} (mm)	14	10	6
λ_{Ti} (mm)	36	26	16
λ_{Ni} (mm)	42	29	18

Considering the scattering effect of the sputtered atoms, Ti atoms have a shorter mean free path than Ni atoms at the same gas pressure. Also, Ti atoms are lighter than Ni atoms (Table 4-1). Thus, there are more significant scattering effects of Ti atoms during the transport process than Ni atoms. Ti atoms are more easily scattered to other places inside the chamber as well as the substrate. Therefore, the Ti concentration in the thin films will decrease with increasing gas pressure. However, the distance between target and substrate was 51 mm, resulting in only slight differences in collision numbers between the sputtered Ti and Ni atoms at the three pressure levels. Therefore, it is questionable that such slight differences in collision numbers can result in the compositional changes shown in Figure 4-14. Also, the scattering effects of the sputtered atoms cannot explain the increasing of Ti concentration when the pressure was increased from 0.44 Pa to 0.64 Pa.

The other factor to consider is the resputtering effect by the neutral atoms. When the pressure increased from 0.44 Pa to 1.01 Pa, the collision number changed from 3 to 8 times. The increasing collision number would reduce the resputtering effect. Therefore, the Ti concentration in the thin films will increase with increasing gas pressure. But, the increasing of collision numbers can also increase the effect of thermalization and the gas becomes rarefield near the cathode, as discussed in section 4.2.3. This rarefaction effect changes the local number of gas atoms that can scatter the sputtered atoms and the neutral atoms. Thus, the increasing pressure (up to 1.0 Pa) increases the rarefaction effect and increases the resputtering effect again. This phenomenon causes more depletion of Ti. So, a maximum Ti (minimum Ni) concentration can be found when increasing from low pressure (0.44 Pa) to high pressure (1.01 Pa). This argument can also explain why at a high pressure region (1.01 Pa) the film deposited at the center position had a comparable composition to that deposited at the off center position, which suffered the sputtering of ion flux.

This test indicates that at pressures lower than 1 Pa, the resputtering effects will dominate the scattering effect of sputtered atoms and determine the final composition results of the TiNi alloys.

4.2.5 Effect of Working Distance

Changing the distance between target and substrate has the same effect of changing gas pressure — both methods change the number of collisions of the sputtered atoms and reflected neutral atoms before they arrive at the substrate. In this test, due to the limitation of the sputtering system configuration, there were two different working distances, 51 mm and 76 mm, being surveyed. Table 4-8 displays the detailed process conditions and their compositional results. The processes were controlled by voltage regulation mode and kept constant at 600 V, and processed at constant pressure, 0.61 Pa. A graph of composition as a function of working distance is shown in Figure 4-15. Note that the composition in thin films deposited at the two different distances was almost the same when considering the effect of measurement error.

From the mean free path equation, Equation (4.8), at pressure 0.61 Pa, the mean free paths for Ar, Ti, and Ni are: $\lambda_{Ar} = 10$ mm, $\lambda_{Ti} = 26$ mm, and $\lambda_{Ni} = 30$ mm. As discussed in above test, the collisions of the neutral atoms determined the compositional results. When working distance increased from 51 mm to 76 mm, the collision number of Ar atoms changed from 5 to 7 times. In this collision region, the change of collision number increased the thermalization effect, and indirectly caused a higher resputtering effect. Therefore, the Ni concentration increased as the working distance increased. However, because the increasing resputtering effect was due to the decrease of local gas density near the cathode, as the working distance increased, this localized span no longer dominated the transport distance. Thus, the total resputtering effect between these two working distances showed no significant difference, nor did the thin film composition.

Due to the limitation of the number of samples, the effect of working distance on TiNi thin film composition cannot be fully exploited. However, in principle, changing the working distance has the same effect as changing the gas pressure. So, the compositional change in thin films due to changing working distance can be explained by the gas pressure effect study.

Distance = 51 mm	600 V, 0.61 Pa, 241→262W, 399→431 mA, time=35 min
Position	At Center Position
Thickness	53,478 Å
Deposition Rate	1528 Å/min
Composition (Ni at%)	51.47±0.33%
Distance = 76 mm	600 V, 0.61 Pa, 281→286 W, 467→474 mA, time=55 min
Position	At Center Position
Thickness	45,376 Å
Deposition Rate	825 Å/min
Composition (Ni at%)	51.79±0.05%
Target Composition (Ni-Ti at%) 50.59 - 49.41 at% ±0.04 Ni	

Table 4-8 Process Conditions and the Compositional Results in the Working Distance Effect Test

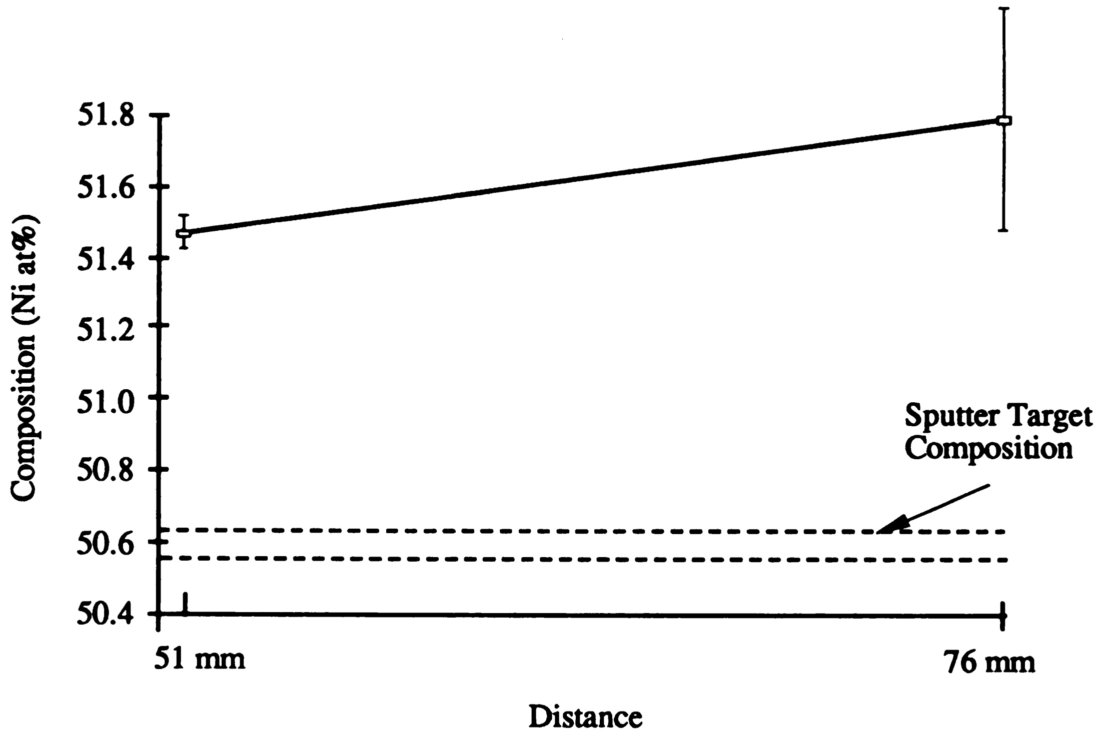

Figure 4-15 Composition Change as a Function of Working Distance

CHAPTER 5 CONCLUSIONS

The purpose of this study is to exploit the process conditions which can fabricate thin films with controllable compositions deviating either positively or negatively from the target alloy composition in magnetron sputter-deposition method. In previous studies, only Ni-rich thin films can be made when using single TiNi target. In the present study, Ti-rich thin films were successfully fabricated by means of controlling the magnetron sputtering process parameters.

In dc magnetron sputtering, the deposition processes are usually operated in argon at a pressure of 0.15 to 1.5 Pa and current densities from 4 to 60 mA/cm^2. Under these process conditions, the resputtering of growing thin films by the reflected neutral atoms is inevitable and has significant effects on the film composition. If TiNi thin films were deposited under steady-state condition, the sputtered flux leaving the target surface with the same composition as the target alloy, the depletion of Ti can be always found in the thin films due to the preferential resputtering of Ti, no matter what the effects of angular distribution and scattering of the sputtered atoms. However, in non-steady-state transition stages, there is a chance that the sputtered flux may carry more Ti component than Ni as compared to that seen under steady-state condition. Thus, a Ti-rich thin film (with respect to the target composition) deposited during the transition periods can be fabricated when the amount of excess Ti can overcome the preferential resputtering.

In the present experiments, the power supply of the sputtering system can be controlled by three regulation modes: voltage, power, or current. When the deposition processes are controlled by voltage regulation mode, steady-state condition can be maintained during deposition. However, when the processes are controlled by power regulation mode, non-steady-state conditions can be setup due to the increasing strength of magnetic fields in the TORUS®-2C magnetron source during deposition. Finally, the ion current densities can affect the target surface topographies, which in turn significantly affect the mechanisms occurring during the transition stages.

Following are listed conclusions of the present study.

(1) A Ti-rich thin film can only be fabricated in the processes controlled by the power regulation mode using the TORUS®-2C magnetron source due to the non-steady-state conditions.

(2) When the process conditions are at 250 W to 350 W, Ti-rich thin films can be fabricated.

(3) The angular distribution and scattering effects of sputtered atoms are possible factors influencing the deposited thin film composition. However, in plasma magnetron sputtering system, they become insignificant and negligible in the analysis when compared to the resputtering effect and the non-steady-state sputtered flux effect.

(4) Under steady-state, Ni concentration in thin films will increase with increasing voltage due to the increasing effect of resputtering.

(5) The change of pressure and working distance alter the significance of the resputtering effect. When thin films are deposited under steady-state condition, the adjustment of pressure and working distance can only reduce the amount of depleted Ti, but never produce a Ti-rich thin film.

(6) At a pressure of 0.64 Pa, the resputtering effect can be reduced to the minimum and a thin film composition close to the target alloy composition can be made.

BIBLIOGRAPHY

BIBLIOGRAPHY

1. C.M. Jackson, H.J. Wagner, and R.J. Wasilewski, NASA Report SP-5110 (1972).
2. H. Funakubo ed., "Shape Memory Alloys", translated by J.D. Kennedy, Gordon and Breach, New York, (1984), 61.
3. A.D. Johnson, J. Micromech. Microeng., 1(1991), 34.
4. D.S. Grummon, S. Nam and L. Chang, in "Shape Memory Materials and Phenomena-Fundamental Aspects and Applications", eds. C.T. Liu, H. Kunsmann, K. Otsuka and M. Wuttig, MRS Symposium Proceedings, Vol. 246, (1991), 259.
5. L.I. Maissel and R. Glang, in "Handbook of Thin Film Technology", eds. L.I. Maissel and R. Glang, McGraw-Hill, New York, (1970), 28.
6. K.N. Melton, in "Engineering Aspects of Shape Memory Alloys", eds. T.W. Duerig, K.N. Melton, D. Stockel and C.M. Wayman, Butterworth-Heinemann, London, (1990), 21.
7. C.M. Wayman and T.W. Duerig, in "Engineering Aspects of Shape Memory Alloys", eds. T.W. Duerig, K.N. Melton, D. Stockel and C.M. Wayman, Butterworth-Heinemann, London, (1990), 3.
8. Binary Alloy Phase Diagrams, Vol. 2, ed. T.B. Massalski, American Metals Society, Metals Park, (1987), 1768.
9. R.J. Wasilewski, S.R. Butler, J.E. Hanlon and D. Worden, Metall. Trans., 2(1971), 229.
10. F.J.J. Van Loo, G.F. Bastin and A.J.H. Leenen, J. Less Common Met., 57, (1978), 11.

11. M. Nishida, C.M. Wayman and T. Honma, Metall. Trans., 17A(1986), 1505.

12. J.J. Kim, P. Moine and D.A. Stevenson, Scripta Metall., 20(1986), 243.

13. T. Sabrui, S. Nenno and T. Fukuda, J. Less Common Met., 125(1986), 157.

14. G. Chattopadhyay and H. Kleykamp, Z Metallkd., 74(1983), 182.

15. C.Y. Xie, L.C. Zhao and T.C. Lei, Scripta Metall., 24(1990), 1753.

16. S. Miyazaki and K. Otsuka, Metall. Trans., 17A(1986), 53.

17. P. Tautzenberger, Conference Proceedings on Engineering Aspects of Shape Memory Alloys, Michigan State University, August (1988).

18. L.M. Schetky, Sci. Am., XX(1979), 74.

19. R. Sachdeva and S. Miyazaki, Conference Proceedings on Engineering Aspects of Shape Memory Alloys, Michigan State University, August, (1988).

20. H.S. Chen, Rep. Prog. Phys., 43(1980), 34.

21. B.X. Liu, W.L. Johnson, M.A. Nicolet and S.S. Lau, in "Nucl. Instrum. Methods", eds. B. Biasse, G. Destefanis and J.P. Gaillard, 209-210(1983), 229.

22. A.K. Rai and R.S. Rhattacharya, Mat. Sci. Engr., 85(1987), 139.

23. B. Walles, L. Chang and D.S. Grummon, in "Shape Memory Materials and Phenomena-Fundamental Aspects and Applications", eds. C.T. Liu, H. Kunsmann, K. Otsuka and M. Wuttig, MRS Symposium Proceedings, Vol. 246, (1991), 349.

24. B.M. Clemens, J. Appl. Phys., 61(1987), 4525.

25. L. Chang and D.S. Grummon, Scripta Metall., 25(1991), 2079.

26. L. Chang, Ph.D dissertation, Michigan State University, (1992).

27. H.H. Anderson and H.L. Bay in "Sputtering by Particle Bombardment I", eds., R. Behrisch, Springer-Verlag, Berlin, (1981), 145.

28. R.V. Stuart and G.K. Wehner, J. Appl. Phys., 33(1962), 2345.

29. J.D. Busch, A.D. Johnson, C.H. Lee and D.A. Stevenson, J. Appl. Phys., 68(1990), 6224.

30. J.D. Busch, M.H. Borkson and A.D. Johnson presented in MRS Meeting at Anaheim (1991).

31. A. Ishida, A. Takei and S. Miyazaki, Thin Solid Films, 228(1993), 210.

32. J.A. Walker, K.J. Gabriel and M. Mehregany, Sensors and Actuators, A21-A23(1990), 243.

33. Joy George, "Preparation of Thin Films", Marcel Dekker Inc., New York, (1992)

34. B. Chapman, "Glow Discharge Processes", John Wiley & Sons, New York, (1980).

35. Leon Maissel, in "Handbook of Thin Film Technology", eds. L.I. Maissel and R. Glang, McGraw-Hill, New York, (1970), Chap. 4.

36. G.K. Wehner and G.S. Anderson, in "Handbook of Thin Film Technology", eds. L.I. Maissel and R. Glang, McGraw-Hill, New York, (1970), Chap. 3.

37. R. Kelly, in "Ion Bombardment Modification of Surfaces", eds. O. Auciello and R. Kelly, Elsevier Science, Amsterdam, (1984), 101.

38. K.D. Leawer and B.N. Chapman, "Thin Films", Wykeham Publications, London.

39. F.A. Green and B.N. Chapman, J. Vac. Sci. Technol. 13(1976), 165.

40. P.K. Waits, in "Thin Film Processes", eds. J.L. Vossen and W. Kern, Academic Press, New York, (1978), 131.

41. G. Betz and G.K. Wehner, in "Sputtering by Particle Bombardment II", eds. R. Behrisch, Springer-Verlag, Berlin, (1983), 11.

42. N.J. Zaluzec, in "Introduction to Analytical Electron Microscopy", eds. J.J. Hren, J.I. Goldstein and D.C. Joy, Plenum Press, New York, (1979), 121.

43. J.C. Russ, "Fundamentals of Energy Dispersive X-ray Analysis", Butterworths & Co Ltd., (1984).

44. S.J.B. Reed, "Electron microprobe Analysis", Cambridge University Press, (1975).

45. N.J. Zaluzec, in "Introduction to Analytical Electron Microscopy", eds. J.J. Hren, J.I. Goldstein and D.C. Joy, Plenum Press, New York, (1979), 83.

46. H.A. Bethe, Ann. Phys. Leipz., 5(1965), 913.

47. J.C. Russ, in "Energy Dispersive X-ray Spectrometry", (NBS 604 op.cit), pp 297.

48. S.J.B. Reed, Brit. J. Apply. Phys., 16(1965), 913.

49 J.G. Miller and D.I. Bolef, J. Appl. Phys., 39(1968), 5815.

50. P. Signund, in "Sputtering by Particle Bombardment I", eds. R. Behrisch, Springer-Verlag, Berlin, (1981), 9.

51. P. Sigmund, J. Appl. Phys., 50(1979), 7261.

52. R. Kelly, Surf. Sci. 100(1980), 85

53. H. Tsuge, S. Esho, J. Appl. Phys., 52(1981), 439.

54. P. Sigmund, Phys. Rev., 184(1969), 383.

55. K. Besocke, S. Berger, W.O. Hofer and U. Littmark, Radiation Effect, 66(1982), 35.

56. J.P. Biersack and W. Eckstein, Appl. Phys., A34(1984), 73.

57. E. Kay, Adv. Electronics and Electron Phys., 17(1962), 245.

58. R.R. Olson, M.E. King, G.K. Wehner, J. Appl. Phys., 50(1979), 3677.

59. G. Carter, B Navinsek and J.L. Whitton, in "Sputtering by Particle Bombardment II", eds. R. Behrisch, Springer-Verlag, Berlin, (1983), 231.

60. G. Carter, J.S. Colligon and M.J. Nobes, J. Mate. Sci., 8(1973), 1473.

61. D.J. Barber, F.C. Frank, M. Moss, J.W. Steeds and I.S.T. Tsong, J. Mate. Sci., 8(1973), 1030.

62. J.L. Whitton, in "Erosion and Growth of Solids Stimulated by Atom and Ion Beam", eds. G. Kiriakidis, G. Carter and J.L. Whitton, Martinus Nijhoff Publishers, (1986), 151.

63. H.R. Kaufman and R.S. Robinson, J. Vac. Sci., 85(1979), 353.

64. S.M. Rossnagel and R.S. Robinson, J. Vac. Sci., 20(1982), 506.

65. U. Littmark and W.O. Hofer, J. Mate. Sci., 13(1978), 2577.

66. J.L. Vossen and J.J. Cuomo, in "Thin Film Processes", eds. J.L. Vossen and W. Kern, Academic Press, New York, (1978), 11.

67. N. Savvides and B. Window, J. Vac. Sci. Technol., A4(3)(1986), 453.

68. B. Window and N. Savvides, J. Vac. Sci. Technol., A4(1986), 196.

69. J.A. Thornton and A.S. Penfold, in "Thin Film Processes", eds. J.L. Vossen and W. Kern, Academic Press, New York, (1978), 76.

70. R. Parsons, in "Thin Film Processes II", eds. J.L. Vossen and W. Kern, Academic Press, New York, (1991), 177.

71. P.S. Ho, Surf. Sci., 72(1978), 253.

72. P.S. Ho, J.E. Lewis, H.S. Wildman and J.K. Howard, Surf. Sci., 57(1976), 393.

73. H.W. Pickering, J. Vac. Sci. Technol., 13(1976), 618.

74. V.E. Henrich and J.C.C. Fan, Surf. Sci., 42(1974), 139.

75. S.D. Dahlgren and E.D. Mcclanahan, J. Appl. Phys., 43(1972), 1514.

76. L.I. Maissel, in "Physics of Thin Films", eds. G. Hass and R.E. Thun, Vol. 3, Academic Press, New York, (1966).

77. D.W. Hoffman, J. Vac. Sci. Technol., A3(1985), 561.

78. S.M. Rossnagel, J. Vac. Sci. Technol., A6(1988), 19.